



SpiLenet based detection and severity level classification of lung cancer using CT images

Lakshmana Rao Vadala ^a, Manisha Das ^b, Ch Raga Madhuri ^c, Suneetha Merugula ^{d,*}

^a Department of Computer Science and Engineering, GVP College of Engineering for Women (A), Visakhapatnam, Andhra Pradesh, India

^b Department of CSE-AIML, GMR Institute of Technology, GMR Nagar, Rajam, Andhra Pradesh, India

^c Department of Computer Science and Engineering, Velagapudi Ramakrishna Siddhartha Engineering College, Vijayawada, Andhra Pradesh, India

^d Department of CSE, GITAM School of Technology, GITAM (Deemed to be University), Visakhapatnam, Andhra Pradesh, India

ARTICLE INFO

Keywords:

Lung cancer
Deep learning (DL)
SpinalNet
Savitzky-Golay (SG) filter
LeNet

ABSTRACT

Lung cancer is the type of cancer, which causes the global mortality. However, predicting and testing remains a serious issue due to its widespread and rapid growth. Hence, this research proposed the SpiLenet for lung cancer detection using computed tomography (CT) scan images. Initially, CT images are taken from a specific dataset, which are pre-processed by Savitzky-Golay (SG) filter. Then, the lung lobe segmentation is performed by Dense-Res-Inception Net (DRINet). Following that, the identification of lung nodule is carried out through a grid-based approach. Feature extraction (FE) is performed to extract key features for further analysis. Finally, lung cancer detection is conducted using SpiLenet, a model created by combining SpinalNet and LeNet. Experimental results demonstrate that SpiLenet achieves an accuracy of 92.10 %, an F-measure of 90.40 %, and a precision of 91.10 %.

1. Introduction

The rapid development of technology and abundant usage of electronic devices cause false mutations that impact the majority of people using a genetic problem that completely changes the lifestyle of humans [1]. The wrong mutated DNA cell generations replace the old ones, which generates the abnormal growth of DNA cells. Due to several factors including exposure to chemical gas, air-breathing, habits of alcohol and so on, the abnormal mutation will occur. Mostly, the tumor may occur in anywhere the human body like the brain, breast, lungs and skin due to the mutation of abnormal cells [2]. In general, cancer is the most hazardous human disease, which includes abnormal cell growth and is widespread inside the human body. However, if it is detected and diagnosed in its initial stages, it can be treated successfully [3]. Commonly worldwide, lung cancer causes mortality among men, while in women it is examined as the third major cause and second most common cause of death. Even though in the United States, the occurrence of lung cancer began to decrease among men, it increased among women [4].

Lung cancer has four phases, such as I to IV [5] that frequently occur due to constant smoking that provides minimal chance of living [6,7]. Currently, CT is more efficacious and popular than plain chest X-rays to diagnose and detect lung cancer. Hence, CT imaging emerges as the best imaging technique, which is robust in diagnosing lung cancer and possibly reveals each suspicious and unsuspicious nodule of lung cancer [5]. An automatic lung cancer prediction model is generated by employing CT images to identify the disease by utilizing numerous conventional measures including noise elimination of image, feature selection, region segmentation,

* Corresponding author.

E-mail addresses: lakshman.vadala@gmail.com (L.R. Vadala), smerugul@gitam.edu (S. Merugula).

cancer feature extraction and cancer categorization [2]. Usually, experts detect lung cancer by executing a CT scan which offers information about tumor location, shape and dimension also it possibly offers test results rapidly without any pain. Thus, it describes the lung details more obviously. Moreover, CT scan offers detailed chest images of patients that enable better lung cancer detection [3].

Recently, deep learning (DL) approaches have attracted a vast area of importance among the computer vision and machine learning (ML) community [8]. In current years, DL's appearance has a crucial effect on medical imaging evolution. Furthermore, in several medical imaging applications, DL is emerged as a promising field, which offers improved executions [9]. DL possibly isolates lung boundaries more efficiently and rapidly. Clinical image specialists are excited to develop lung cancer identification schemes based on DL techniques. However, these kinds of approaches require more period to process, which is sensitive to boundaries [10]. However, in recent times, there are several inquiries have been investigated in deep networks to identify lung pathology [8]. Generally, Convolution neural networks (CNNs) describe their influence on object-recognition weakness and have been employed for Personal Computer (PC) vision assignments within DL strategies. Hence, it has been implemented in several image classification techniques. Therefore, CNN is employed for analyzing the detection of lung cancer [10]. Moreover, general computer-aided diagnosis (CAD) techniques utilise the features that are associated with cancer suspicion including dimension, solidity, volume, shape and so on [11]. However, DL is considered a fundamental image segmentation approach that possibly isolates the interstitial lung boundaries more efficiently and rapidly [12]. Besides, several techniques have utilized DL approaches, which efficaciously diagnose lung disease and greatly handle clinical image assessment issues [10]. Hence, most of the lung segmentation frameworks utilize DL-based approaches, which provide better performances in numerous fields [13].

1.1. Problem statement

Lung cancer is the deadliest forms of cancer, with high mortality rates due to late-stage diagnosis. Previous research has implemented various methods for Lung Cancer detection. However, these methods face several common challenges, including:

- Medical imaging data can vary significantly due to differences in equipment, resolution, and acquisition protocols. This variability can make it challenging for deep learning models to generalize across different institutions or populations in past studies.
- In prior research, early detection models frequently faced challenges with false positives and false negatives. Both types of errors can have severe consequences for patient outcomes.
- In previous research, lung cancer was often diagnosed at an advanced stage due to the absence of early symptoms, which complicates treatment and reduces survival rates.

These problems are addressed by developing the SpiLenet model for the identification of Lung cancer in this research.

The crucial intention is to detect Lung cancer by utilizing SpiLenet. Initially, input CT images obtained from the datasets, which are preprocessed by SG filter. Subsequently, the segmentation is carried out by DRINet. Following this, FE takes place. Last, Lung cancer is identified using SpiLenet that is modeled by merging SpinalNet and LeNet.

The main contribution is portrayed as,

- **Proposed SpiLenet for Lung Cancer Detection:** The lung cancer detection is done by developing the SpiLenet model, which is formed by the combination of SpinalNet and LeNet.
- The segmentation is performed using DRINet, while lung nodule identification is performed through a grid-based scheme.

The rest of the divisions are organized as: the reviewed papers is demonstrated in [Section 2](#), the proposed SpiLenet method is portrayed in [Section 3](#), the attained outcomes for SpiLenet is described in [Section 4](#), and the conclusion part of SpiLenet is represented in [Section 5](#).

2. Motivation

In general, the most crucial cause of Lung cancer is late detection at its severe stage. It can be cured when it is identified at its initial stage. Nonetheless, when Lung cancer is not identified in advance, it will decrease the survival rate of the patient. Moreover, it is difficult to diagnose Lung cancer at the initial stages, which inspires researchers to introduce an efficacious approach.

2.1. Literature survey

Shakeel, P.M., et al. [2] introduced an enhanced deep neural network (DNN) for automatic lung cancer identification. This method processed the input images using a multilevel brightness-preserving method. This approach achieved robustness by utilizing the collective decision-making of various classifiers. However, the model's computational time for cancer recognition was quite high. Alzubaidi, M.A., et al. [3] devised a local feature extraction framework for detecting lung cancer. This approach was beneficial for identifying suspicious areas by employing CT scan images. Also, this model aided radiologists in identifying lung cancer, but it failed to examine more comparison algorithms and further, it did not include enormous amounts of datasets. Jena, S.R., et al. [8] designed a Deep Gaussian mixture model in a region-based convolutional neural network (DGMM-RBCNN) to detect and classify lung cancer. In this model, the Gaussian and Wiener filters were utilized to remove the Gaussian noise. This scheme had achieved lower computational time. However, it failed to expand this approach to other cancer kinds like brain, breast and so on. Nazir, I., et al. [13] developed an

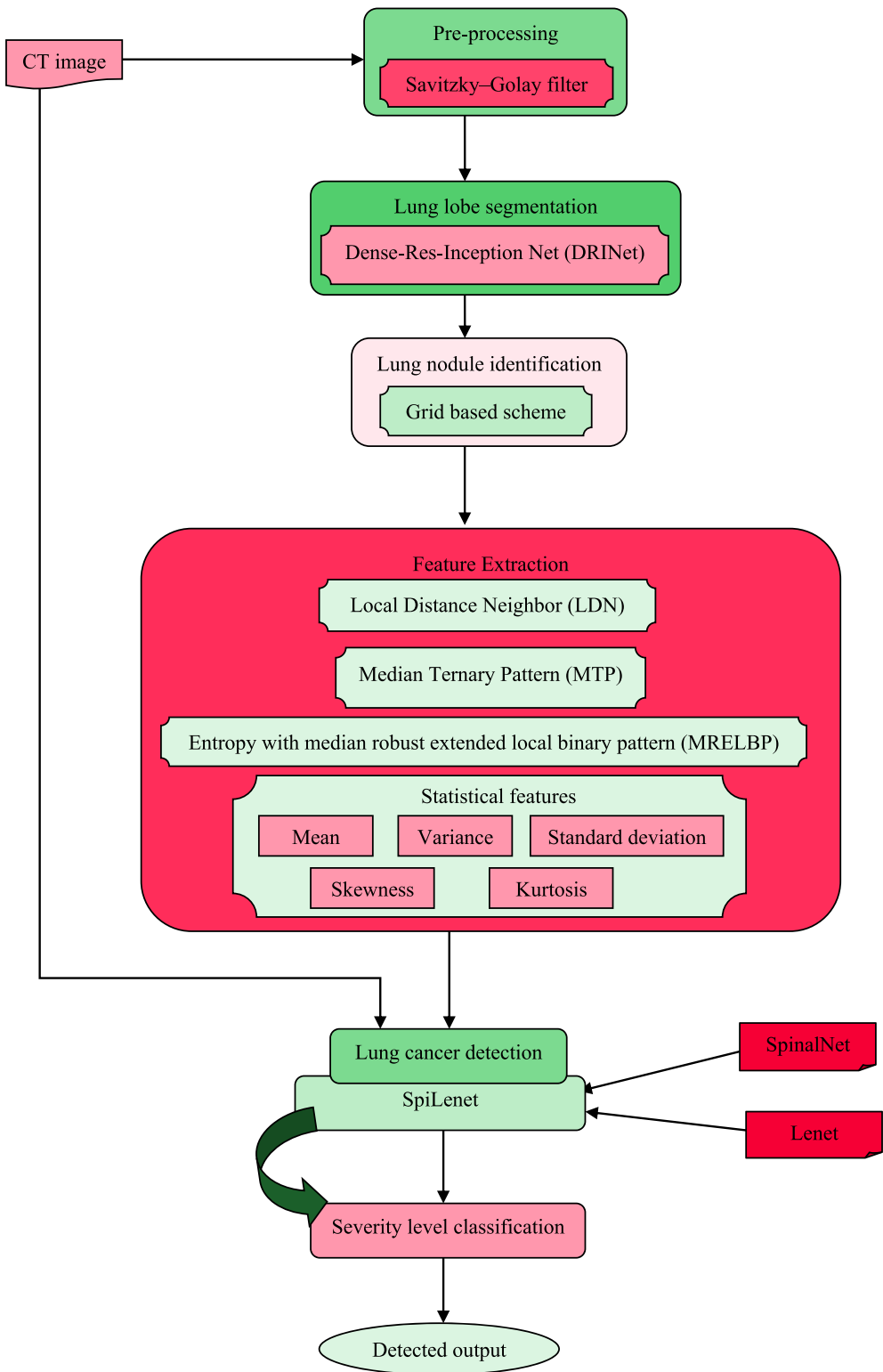


Fig. 1. Diagrammatic representation of SpiLenet for lung cancer detection.

Image fusion technique for lung cancer identification. This strategy attained minimal time complexity by enhancing the quality of the image and eliminating image noise, but it failed to estimate the method on the enormous dataset to get enhanced robustness.

Tiwari, L., et al. [10] modeled Deep convolution neural network (DCNN) to identify lung cancer. Here, the advanced learning-based paradigm with various approaches was employed to accurately analyze the critical nodules. This technique had precisely detected lung nodules in complicated CT scans. Although, it did not provide more information about several tumors. Bishnoi, V., et al. [7] designed a Hybrid Sequential Exhaustive Feature Selection (HSEFS) for lung cancer diagnosis. This model compared with three algorithms to assess the optimal feature score. Moreover, this approach was appropriate for enormous datasets, but it had higher computational time which makes the system more complicated. Vijh, S., et al. [9] introduced a Hybrid whale optimization algorithm-based adaptive particle swarm optimization (WOA_APSO) algorithm for automatic lung cancer detection. Here, the preprocessing and segmentation were applied to lung CT images to get the segmented tumor and non-tumor regions. This approach was efficient, reliable and had minimal computation cost. However, it failed to involve other metaheuristic approaches for enhancing the system's performance. Tiwari, L., et al. [14] developed Target target-based Weighted Elman DL Neural Network (TWEDLNN) for identifying lung nodules and cancer. In this approach, the lung image segmentation was performed by using the contrast enhancement (CE) and Geometric Mean-based Otsu Thresholding (GOT). This approach was more advanced and uncomplicated. Nonetheless, it had attained higher computational complexity.

2.2. Issues

The previous research issues are examined below:

- Even though the devised approach in [2] provided better quality lung images and efficiently removed noises from CT images, the system's dimensionality was minimized due to the implementation of spiral settings.
- The devised model in [10] was efficaciously reliable by handling CT scan variations with diverse parameters. However, it did not provide a sufficient supply of both the normal and tumor lung images, which is essential for reliable system performance.
- HSEFS in [7] was introduced to detect lung cancer. Although this technique required a lower training period, it was unable to expand the assessment of other feature selection approaches for the feature selection process.
- Recently, lung cancer has emerged as the most dangerous disease worldwide, which affects both men as well as women and possibly maximizes the death rate among cancer cases. Nonetheless, it is considered a difficult process to detect the growth of cancer.

3. Designed SpiLeNet for lung cancer detection

This work designed an efficacious model named SpiLeNet for lung cancer detection. Initially, CT images are acquired from the specific dataset [15] and are fed into a pre-processing module using an SG filter [16] to reduce noise. After pre-processing, lung lobe segmentation is carried out using DRINet [17]. Subsequently, the lung nodule identification is done using a grid-based scheme [18]. Following this, FE takes place. Therefore, the extracted features are Local Distance Neighbor (LDN) [19], Median Ternary Pattern (MTP) [20], Entropy with median robust extended local binary pattern (MRELBP) [21] and statistical features that include mean, variance, standard deviation, skewness and kurtosis. At Last, Lung cancer detection using CT images is executed utilizing SpiLeNet, which is the combination of SpinalNet [22] and LeNet [23] where layers are modified using the fuzzy concept. Moreover, severity level classification is executed by SpiLeNet. Fig. 1 demonstrates a diagrammatic representation of lung cancer detection using SpiLeNet.

3.1. Image acquisition

Assuming input image database as I that involves \aleph quantity of input images, which is described as,

$$I = \{I_1, I_2, \dots, I_\kappa, \dots, I_\aleph\} \quad (1)$$

Here, I represents the database, \aleph indicates an entire number of images in I and I_κ refers κ^{th} number of images in I .

3.2. Pre-processing utilizing SG filter

In this phase, the pre-processing is done using SG filtering. SG filtering is employed to remove noises from input images and also calculates and smooths a series of consecutive derivative values. It is well-known for its ability to smooth data while preserving important features such as peaks and edges. Also, the SG filter uses a polynomial fitting approach over a moving window, which allows for more sophisticated smoothing compared to simple convolution-based filters. Next, it handles fine-scale variations in the data making it more suitable for high-resolution imaging. The input I_κ is delivered into a preprocessing phase that is executed by SG filtering that provides a preprocessed outcome P_κ . Applying the smoothing process in SG filtering which is described as:

$$G_s^* = \frac{\sum_{p=-h}^{p=h} A_p G_{s+l}}{\Lambda} \quad (2)$$

Here, Λ specifies the amount of data points in the smoothing window, where h is its half-width, G and G^* refers original and

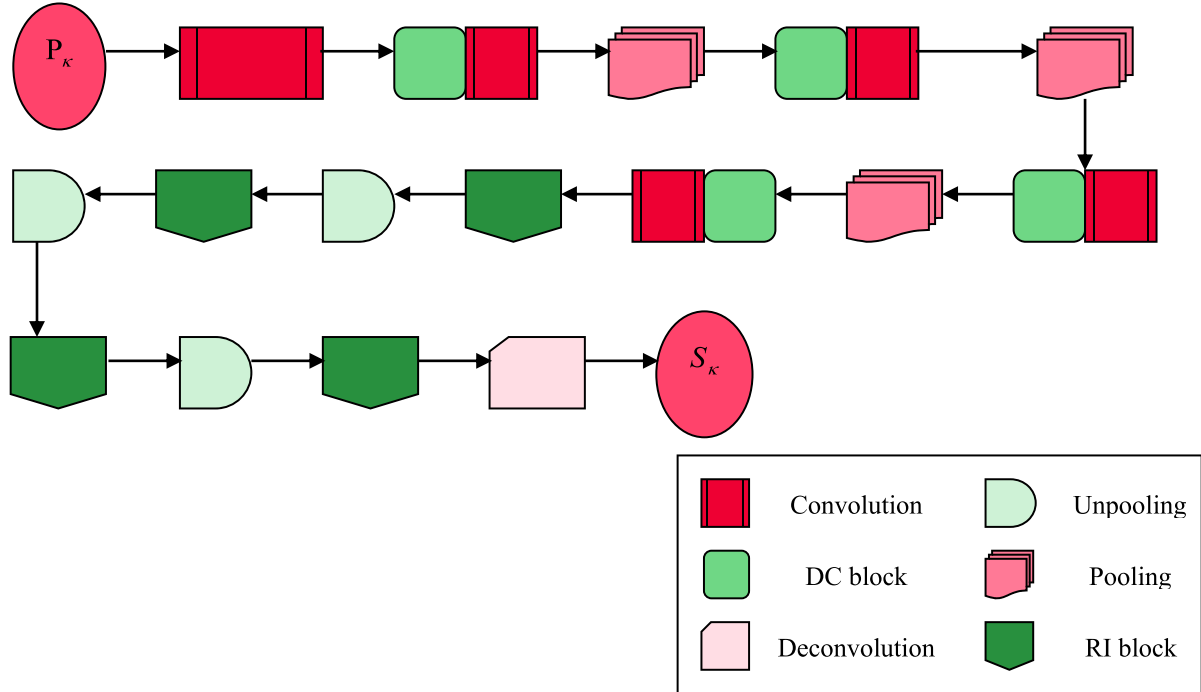


Fig. 2. Architecture of DRINet.

smoothed signal, s describes the ordinate data's running index, A_p represents the coefficient of p^{th} smoothing. Hence in least-squares valuation, the polynomial is modeled as,

$$x_a(p) = l_0 + l_1 p + l_2 p^2 + \dots + l_a p^a = \sum_{r=0}^a l_r p^r, \quad p \leq 2h \quad (3)$$

Here, l_r and a denotes coefficient and polynomial degree. SG algorithm acquires unknown filtering coefficients l_r , and it is formulated as:

$$\frac{\partial}{\partial l_r} \left[\sum_{p=-h}^h (x_a(p) - G_p) \right] = 0 \quad (4)$$

When $p = 0$ r^{th} differential of Eq. (3) is estimated to obtain l_r , which is assumed as:

$$x_a'(0) = \sum_{p=-h}^h A_p^r G_p \quad (5)$$

Here A_p^r and G_p demonstrates convolution weights and value of p^{th} points, and r refers to derivative order. The pre-processed outcome is represented as P_κ .

3.3. Segmentation using DRINet

Lung lobe segmentation plays a significant role in medical diagnosis, which divides the lungs into anatomically different regions for accurate surgical planning. Hence, in this phase lung lobe segmentation is conducted by DRINet, which is simple and flexible and effectively manages parameter space and performance. Moreover, it handles challenging clinical segmentation issues, and it maintains the efficiency of computation. Its architecture helps in reducing false negatives and false positives, which is a common issue in lung cancer detection. By leveraging multi-scale features, dense connections, and residual learning, DRINet improves the accuracy of segmentation, making it more reliable for clinical decision-making. Furthermore, the dense connections in DRINet allow the network to better capture subtle features, including low-contrast or poorly delineated nodules, which are common in early lung cancer detection. This means DRINet can outperform traditional models in recognizing early or hidden tumors that may be hard to differentiate from the surrounding lung tissue. Here, a pre-processed outcome P_κ is introduced into DRINet that delivers a segmented output S_κ . DRINet contains an analysis and synthesis path in which the analysis path consists of a dense connection block and the synthetic path involves residual inception and unpooling block. Fig. 2 describes the architecture of DRINet.

3.3.1. Dense connection block

Considering $\lambda_i^N = (i-1)/(N-1)$, $i = 1, 2, \dots, N$ as an input for n^{th} layer and $d(\cdot)$ represents a convolution function. Thus, the standard convolution layer is given as,

$$g_{n+1} = d(g_n) \quad (6)$$

whereas, dense convolution block is demonstrated as:

$$g_{n+1} = d(g_n) \circ g_n \quad (7)$$

where \circ denotes concatenation, g_{n+1} indicates dense convolution block.

3.3.2. Residual inception block

As long as this block learns a function with input maps as a reference, the residual connections make the learning simple. Assume $f(\cdot)$ as a deconvolution function that follows ReLU and BN. The obtained outcome is given by:

$$g_{n+1} = f_q(f_w(g_n) \circ f_q(g_n)) \circ f_w(f_q(g_n)) + g_n \quad (8)$$

where, $f_w(\cdot)$ and $f_q(\cdot)$ denotes dilated deconvolution and bottleneck.

3.3.3. Un-pooling block

In this block, it assimilates up-sampled feature maps from two branches. Consider $f^2(\cdot)$ a deconvolution function and thus up-sampled feature map is demonstrated by,

$$g_{n+1} = f^2(f_q(g_n)) \circ f^2(f_w(f_q(g_n))) \quad (9)$$

Separately up-sampling these feature maps and assimilating them together possibly decreases error effects.

3.4. Detection of lung nodule by a grid-based scheme

In this phase lung nodule identification process is conducted using a grid-based scheme. Grid-based method efficaciously demonstrates whether the nodule area is affected or not, and also it splits segments region into several blocks called grids for lung nodule determination and possibly decreases computational time. Here, S_κ is subjected to a lung nodule identification process that delivers an output N_κ .

3.5. Feature extraction

FE is employed as a crucial concept that combines the features efficaciously and greatly deals with enormous datasets, and also it requires minimal computational effort. Here, the identified output N_κ is subjected to the FE procedure. The extracted features include LDN, MTP, MRELBP and statistical features.

3.5.1. LDN

LDN [24] is more reliable, opposes noise and a six-bit binary code, is allocated to every input image's pixel that represents the texture's structure, and encodes the directional information of the image's textures. LDN is denoted as Φ . Hence, to encode important regions, a permanent position for top positive directional numbers is assigned. Therefore, the code is demonstrated by:

$$\Phi(j, k) = 8t_{j,k} + c_{j,k} \quad (10)$$

where, the central pixel of the coded neighbourhood is represented as (j, k) , the directional amount of increased positive and negative response is described as $t_{j,k}$ and $c_{j,k}$, which is defined as,

$$t_{j,k} = \underset{t}{\operatorname{argmax}}\{\Sigma^t(j, k) | 0 \leq t \leq 7\} \quad (11)$$

$$c_{j,k} = \underset{c}{\operatorname{argmax}}\{\Sigma^c(j, k) | 0 \leq c \leq 7\} \quad (12)$$

Here X is the original image, convolution X is represented as Σ^t , Σ^t denotes the t^{th} mask which is given by

$$\Sigma^t = X * Y^t \quad (13)$$

To generate LDN code, a compass mask is required to estimate edge responses. Hence, the skewed Gaussian derivative generates an asymmetric compass mask to estimate edge response. Hence, the Gaussian mask is formulated as,

$$Z_\eta(j, k) = \frac{1}{2\pi\eta^2} \exp\left(-\frac{j^2 + k^2}{2\eta^2}\right) \quad (14)$$

where η is Gaussian bell's width, j and k represents positions of location. Finally, the mask is described by,

$$Y_\eta(j, k) = Z'_\eta(j + \beta, k) * Z_\eta(j, k) \quad (15)$$

Here Z'_η is a derivative of Z_η , $*$ denotes convolution operation, β specifies the offset of Gaussian. LDN is referred to as F_1 .

3.5.2. MTP

MTP [25] is more robust to noise, which is represented by φ and extracts accurate information. Thus, MTP is expressed by,

$$Q_\varphi(z) = \begin{cases} 1, & z > R_\alpha + \gamma \\ 0, & R_\alpha - \gamma \leq z \leq R_\alpha + \gamma \\ -1, & z < R_\alpha - \gamma \end{cases} \quad (16)$$

where, z denotes the neighbor gray level, γ and R_α refers to the user-specified threshold and local median. Every MTP code divides into E_φ and W_φ and treated as two separate binary patterns, which are computed as follows,

$$\ell^\infty = 1/(N - 1) \quad (17)$$

$$Q_E(z) = \begin{cases} 1, & z = 1 \\ 0, & \text{otherwise} \end{cases} \quad (18)$$

$$W_\varphi = \sum_{\rho=0}^7 Q_W(Q_\varphi(o_\rho)) \times 2^\rho \quad (19)$$

$$Q_W(z) = \begin{cases} 1, & z = -1 \\ 0, & \text{otherwise} \end{cases} \quad (20)$$

where R_α specifies the local neighborhood's median, γ describes the margin threshold, E_φ and W_φ represents positive and negative binary pattern codes. MTP is represented as F_2 .

3.5.3. MRELBP

MRELBP is obtained from the Extended Local Binary Pattern (ELBP). It is expressed as,

$$\tau_C(L_\Delta) = h_j(\varphi_i(\Phi_{\Gamma\Delta,\varphi_\partial}) - \sigma_{\varphi_\partial}) \quad (21)$$

$$\tau_{N,A,G}(L_\Delta) = \sum_{K=0}^{G-1} h_j(\varphi_i(\Phi_{\Gamma A,G,\varphi_{\partial A},K}) - \sigma_{A,G,\varphi_{\partial A}}) * 2^K \quad (22)$$

Where,

$$h_j(L) = \begin{cases} 0, & h_j L \Phi_\Gamma < 0 \\ 1, & h_j L \Phi_\Gamma \geq 0 \end{cases} \quad (23)$$

$$\sigma_{A,G,\varphi_{\partial A}} = \frac{1}{G} * \sum_{K=0}^{G-1} \varphi_i(\Phi_{\Gamma A,G,\varphi_{\partial A},K}) \quad (24)$$

Here, τ_C denotes MRELBP_CI, $\varphi_i(\Phi_{\Gamma\Delta})$ indicates the median value of $\Phi_{\Gamma\Delta}$, $\Phi_{\Gamma\Delta,\varphi_\partial}$ represents the neighborhood of size φ_∂ which is centered on a central pixel L_Δ , $\sigma_{\varphi_\partial}$ specifies average of $\varphi_i(\Phi_{\Gamma\Delta,\varphi_\partial})$, $h_j(L_\Delta)$ represents sign function, $\Phi_{\Gamma A,G,\varphi_{\partial A},K}$ is neighborhood size of $\varphi_{\partial A}$ which is centered on neigchoring pixel $\Phi_{\Gamma A,G,K}$ and G indicates the number of neighbors.

Here entropy is applied with MRELBP, which is obtained as a feature vector and is specified as F_3 .

3.5.4. Statistical features

The extracted statistical features [26] consist of mean, variance, standard deviation, skewness and kurtosis.

3.5.4.1. Mean.

Its distribution generates concentration of data and it is computed as:

$$\mathfrak{J}_1 = \sum_{\beta=0}^{\nu_1-1} \beta * K(\beta) \quad (25)$$

3.5.4.2. Variance.

Its value of deviation associated with the grey level of the mean, and it is denoted as

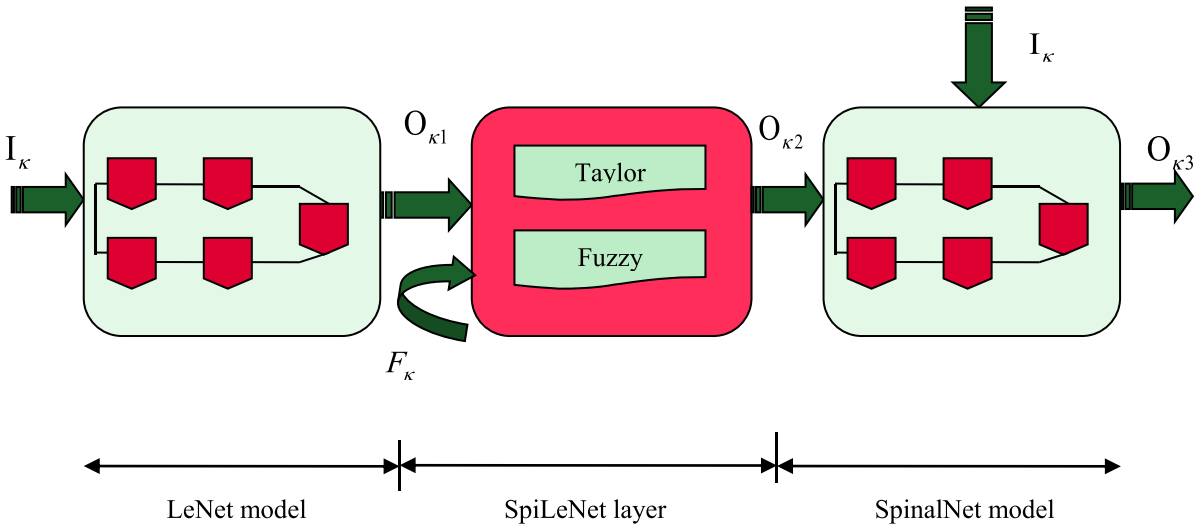


Fig. 3. The general architecture of SpiLenet.

$$\mathfrak{I}_2 = \sum_{\beta=0}^{\nu_i-1} (\beta - \pi)^2 * K(\beta) \quad (26)$$

3.5.4.3. Standard deviation. It is also called the root of variance that is formulated by,

$$\mathfrak{I}_3 = \sqrt{\sum_{\beta=0}^{\nu_i-1} (\beta - \pi)^2 * K(\beta)} \quad (27)$$

3.5.4.4. Skewness. It is the asymmetric of definite distribution feature around the mean, which is formulated by:

$$\mathfrak{I}_4 = \pi^{-3} \left[\sum_{\beta=0}^{\nu_i-1} (\beta - \pi)^3 * K(\beta) \right] \quad (28)$$

3.5.4.5. Kurtosis. It estimates distribution leveling related to a normal distribution, which is expressed as:

$$\mathfrak{I}_5 = \pi^{-4} \left[\sum_{\beta=0}^{\nu_i-1} (\beta - \pi)^4 * K(\beta) \right] \quad (29)$$

Now, applying all statistical features over LDN and MTP, features are computed as:

$$F_1 = \{\mathfrak{I}_1, \mathfrak{I}_2^1, \mathfrak{I}_3^1, \mathfrak{I}_4^1, \mathfrak{I}_5^1\} \quad (30)$$

$$F_2 = \{\mathfrak{I}_1^2, \mathfrak{I}_2^2, \mathfrak{I}_3^2, \mathfrak{I}_4^2, \mathfrak{I}_5^2\} \quad (31)$$

Where, F_1 and F_2 indicates LDN and MTP features.

Thus, the vector of feature is finally computed as,

$$F_k = \{F_1, F_2, F_3\} \quad (32)$$

3.6. Identification of lung cancer utilizing SpileNet

Lung cancer is examined as the dangerous cancer kind, which causes cancer mortality among humans. However, earlier diagnosis of cancerous cells is a better manner to maximize the patient's survival rate. Moreover, several conventional techniques failed to predict cancerous cells at their initial stage. Hence, for reducing these kinds of issues an effective scheme named SpiLenet is implemented to detect the Lung cancer. Here, the input image I_k is given to the LeNet layer, which provides an output O_{k1} . Next, the output of LeNet O_{k1} along with extracted features F_k are subjected to a SpiLenet layer that involves Taylor and fuzzy process and thus provides an output O_{k2} . Moreover, the gained output O_{k2} and input image I_k such that $\Xi_k \in \{I_k, O_{k1}\}$ are then given to the SpinalNet model and provide a final output O_{k3} . Fig. 3 describes the general outline of Spine-Fuzzy-Lenet.

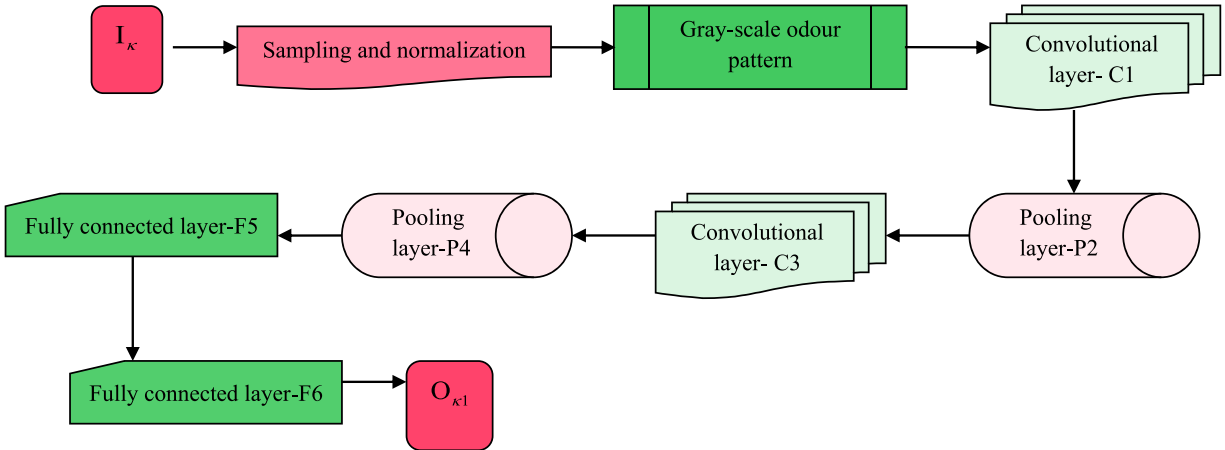


Fig. 4. General structure of LeNet.

3.6.1. LeNet model

LeNet [27] is a classic DL architecture originally designed for handwritten digit recognition, but it has since been adapted for various image recognition tasks, including medical image analysis. It uses convolutional layers to capture hierarchical features, starting from low-level edges and textures to higher-level structures, making it effective in distinguishing cancerous from non-cancerous tissue. Also, it is capable of handling large volumes of lung scan data, which is particularly important in high-throughput screening programs, allowing it to be applied in large-scale clinical settings.

In this phase, I_κ is given to the LeNet model that provides an output $O_{\kappa 1}$, which is employed for multiple classification procedures that are given as,

$$O_{\kappa 1} = \text{softmax}(\chi^\Phi \cdot I_\kappa + \varphi^\Phi) \quad (33)$$

where χ^Φ indicates convolutional kernel, φ^Φ specifies offset term, I_κ refers to the input image.

Fig. 4

3.6.2. SpiLenet layer

Assume, a pattern of two-dimension $[0, 1] \times [0, 1]$ for graphical illustration development [28]. Here, the acquired output $O_{\kappa 1}$ and feature vector F_κ are fed into the Spinal-Fuzzy-Lenet layer that provides an output $O_{\kappa 2}$. Consider Φ_Φ patterns $\partial_\alpha = (\partial_{\alpha 1}, \partial_{\alpha 2}, \dots, \partial_{\alpha \Phi_\Phi})$, $\alpha = 1, 2, \dots, \Phi_\Phi$ with Σ classes ($\zeta 1$: Class 1, $\zeta 2$: Class 2), ..., $\zeta \Sigma$: Class Σ .

By Taylor Concept,

$$\partial(o+1) = \partial(o) + \frac{\partial'(o)}{1!} \quad (34)$$

$$\partial'(o) = \frac{\partial(o) - \partial(o-\hbar)}{\hbar} \quad (35)$$

Assume, $\hbar = 1$ and substitute $\partial'(o)$ in Eq. (34)

$$\partial(o+1) = \partial(o) + \frac{\partial(o) - \partial(o-1)}{1!} \quad (36)$$

$$\partial(o+1) = 2 \cdot \partial(o) - \partial(o-1) \quad (37)$$

$$\partial_\alpha = 2 \cdot F_\kappa - O_{\kappa 1} \quad (38)$$

Here F_κ and $O_{\kappa 1}$ represents the feature vector and output from the previous layer.

3.6.2.1. Fuzzy concept

Consider an axis's pattern space as \aleph ($\aleph \geq 2$). $\nu_i^\aleph(\varpi)$ be the membership function of ε_i^\aleph is described by,

$$\nu_i^\aleph(\varpi) = \max\{1 - |\varpi - \lambda_i^\aleph| / \ell^\aleph, 0\}, \quad i = 1, 2, \dots, \aleph (\aleph \geq 2) \quad (39)$$

$$\lambda_i^\aleph = (i-1)/(\aleph-1), \quad i = 1, 2, \dots, \aleph \quad (40)$$

$$\ell^\aleph = 1/(\aleph-1) \quad (41)$$

Since $\aleph = 1$ ε_1^1 is defined as:

$$\nu_1^1(\varpi) = \begin{cases} 1 & \text{if } 0 \leq \varpi \leq 1, \\ 0 & \text{otherwise.} \end{cases} \quad (42)$$

3.6.2.2. Rule generation. It involves two procedures. When $\partial_{\alpha 1}$ is ε_m^M and $\partial_{\alpha 2}$ is ε_e^E then $(\partial_{\alpha 1}, \partial_{\alpha 2})$ refers to Class $\zeta\omega_{me}^{ME}$ with $\zeta\omega = \zeta\omega_{me}^{ME}$, $m = 1, 2, \dots, M$; $M = 1, 2, \dots, M_{\max}$; $e = 1, 2, \dots, E$; $E = 1, 2, \dots, E_{\max}$ (43)

where Δ_{me}^{ME} refers fuzzy rule label, $\zeta\omega_{me}^{ME}$ indicates classes of Σ_Σ and $\zeta\omega_{me}^{ME}$ represents the fuzzy rule label's certainty, $\varepsilon_m^M \times \varepsilon_e^E$ is a fuzzy subspace.

3.6.2.1.1. Step 1: Fuzzy rules generation.

1) Compute $\mu_{\zeta\theta}$ for $\theta = 1, 2, \dots, \Sigma_\Sigma$ as

$$\mu_{\zeta\theta} = \sum_{\partial_\alpha \in \zeta\theta} \nu_m^M(\partial_{\alpha 1}) \times \nu_e^E(\partial_{\alpha 2}) \quad (44)$$

2) Find Class $\nabla(\zeta\nabla)$,

$$\mu_{\zeta\nabla} = \max\{\mu_{\zeta 1}, \mu_{\zeta 2}, \dots, \mu_{\zeta \Sigma_\Sigma}\} \quad (45)$$

when a single class occupies a larger value, $\zeta\omega_{me}^{ME}$ is specified as Class $\nabla(\zeta\nabla)$

3) When a single class occupies maximum value $\zeta\omega_{me}^{ME}$ is described by,

$$\zeta\omega_{me}^{ME} = (\mu_{\zeta\nabla}) / \left(\sum_{\theta=1}^{\Sigma_\Sigma} \mu_{\zeta\theta} \right) \quad (46)$$

where,

$$\mu = \sum_{\substack{\theta=1 \\ \zeta\theta \neq \zeta\nabla}}^{\Sigma_\Sigma} \mu_{\zeta\theta} / (\Sigma_\Sigma - 1) \quad (47)$$

A set of all generated fuzzy rules is defined by κ_{all} fuzzy rules in each partition, represented as κ^{ME}

$$\kappa_{all} = \{\Delta_{me}^{ME} : m = 1, 2, \dots, M; M = 1, 2, \dots, M_{\max}; e = 1, 2, \dots, E; E = 1, 2, \dots, E_{\max}\} \quad (48)$$

where, κ_{all} represents the rule set.

$$\kappa^{ME} = \{\Delta_{me}^{ME} : m = 1, 2, \dots, M; e = 1, 2, \dots, E\}, \quad M = 1, 2, \dots, M_{\max}; E = 1, 2, \dots, E_{\max} \quad (49)$$

where, κ^{ME} indicates a set of fuzzy rules.

The complete set of fuzzy rules is defined as:

$$\kappa_{all} = \bigcup_{M=1}^{M_{\max}} \bigcup_{E=1}^{E_{\max}} \kappa^{ME} \quad (50)$$

3.6.2.3. New pattern classification. Consider a subset κ of the rule set. In κ a new pattern $\partial_\alpha = (\partial_{\alpha 1}, \partial_{\alpha 2})$.

3.6.2.3.1. Step 2: new pattern classification.

1) Compute $\delta_{\zeta\theta}$ for $\theta = 1, 2, \dots, \Sigma_\Sigma$ as

$$\delta_{\zeta\theta} = \max\{\nu_m^M(\partial_{\alpha 1}) \times \nu_e^E(\partial_{\alpha 2}) \times \zeta\omega_{me}^{ME} : \zeta\omega_{me}^{ME} = \text{Class } \theta \text{ and } \Delta_{me}^{ME}\} \quad (51)$$

2) Find a Class $\nabla(\zeta\nabla)$ such that

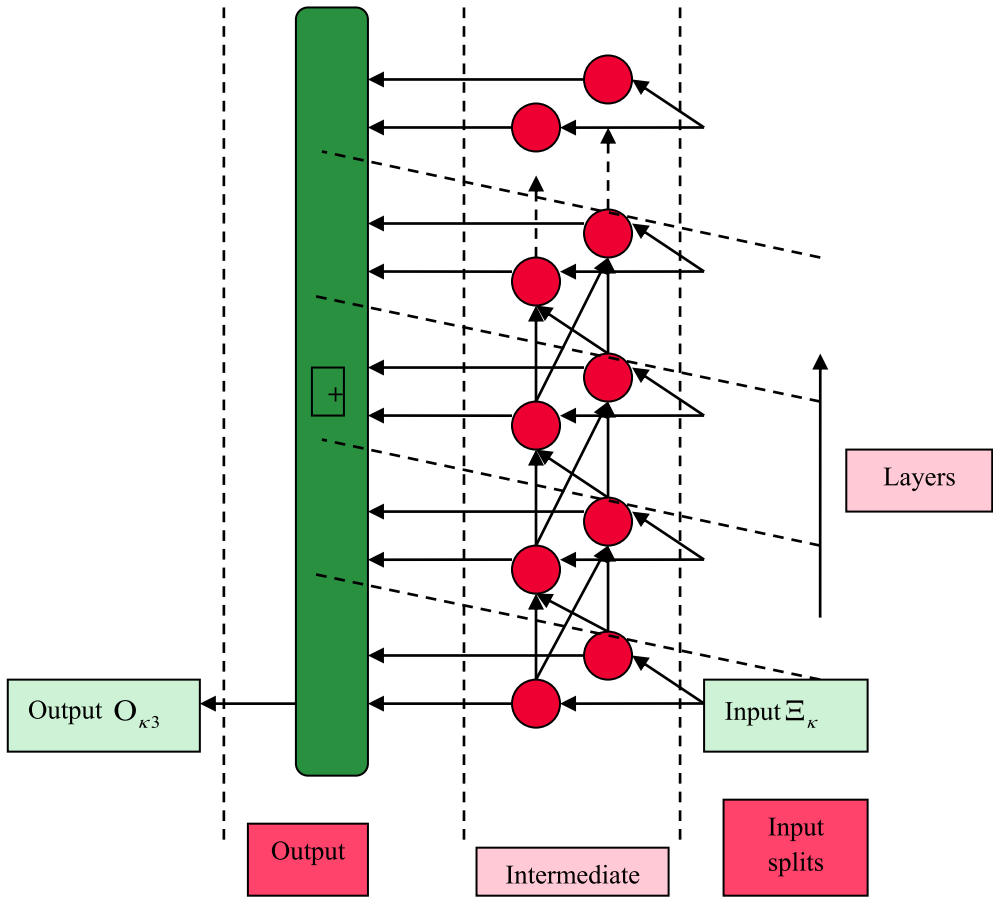


Fig. 5. Architecture of SpinalNet.

$$\delta_{\zeta\nabla} = O_{\Re2} = \max\{\delta_{\zeta1}, \delta_{\zeta2}, \dots, \delta_{\zeta\Sigma}\} \quad (52)$$

The inferred class has the highest value of $\nu_m^M(\partial_{\alpha1}) \times \nu_e^E(\partial_{\alpha2}) \times \zeta o_{me}^{ME}$ amongst all fuzzy rules κ .

3.6.3. SpinalNet model

SpinalNet [29] is a DL architecture designed to enhance the accuracy and efficiency of various image recognition tasks, including medical imaging for lung cancer detection. Its architecture minimizes the number of parameters compared to other deep networks, making it computationally efficient. This is particularly beneficial when working with large medical imaging datasets, as it can help reduce training times and memory requirements. Also, the SpinalNet model can accurately localize cancerous nodules in lung images, a key requirement for early diagnosis and treatment planning. Its architecture is designed to focus on relevant features while discarding less useful data, which enhances its ability to detect nodules and classify them effectively. Additionally, the SpinalNet can be combined with other models or techniques, such as Fuzzy Logic, to improve its decision-making capabilities, which also enhances the accuracy by enabling more nuanced reasoning. SpinalNet includes input, intermediate and output layers. Here, Ξ_κ is fed into the SpinalNet model that gives a final output $O_{\Re3}$. Fig. 5 shows the architecture of SpinalNet. The output in the hidden layer is given as:

$$O_{\Re3} = \varsigma \left(\sum_{\phi=1}^{\Gamma_\Gamma} (\psi_{\Omega\phi}) O_{\Re2} + \Psi_{\Omega}^{\kappa\Omega\ell} \right) \quad (53)$$

where, ς denotes the activation function, Γ_Γ and $\psi_{\Omega\phi}$ indicates the number of neurons and their weight, $\Psi_{\Omega}^{\kappa\Omega\ell}$ specifies neuron's threshold value, $O_{\Re2}$ output from a prior layer.

Table 1
Details of Parameter.

Parameters	Values
	SpinalNet
Batch Size	64
Epoch	100
Hidden neurons	20
Learning rate	0.001
	Lenet
Batch Size	32
Epoch	100
Learning rate	0.001

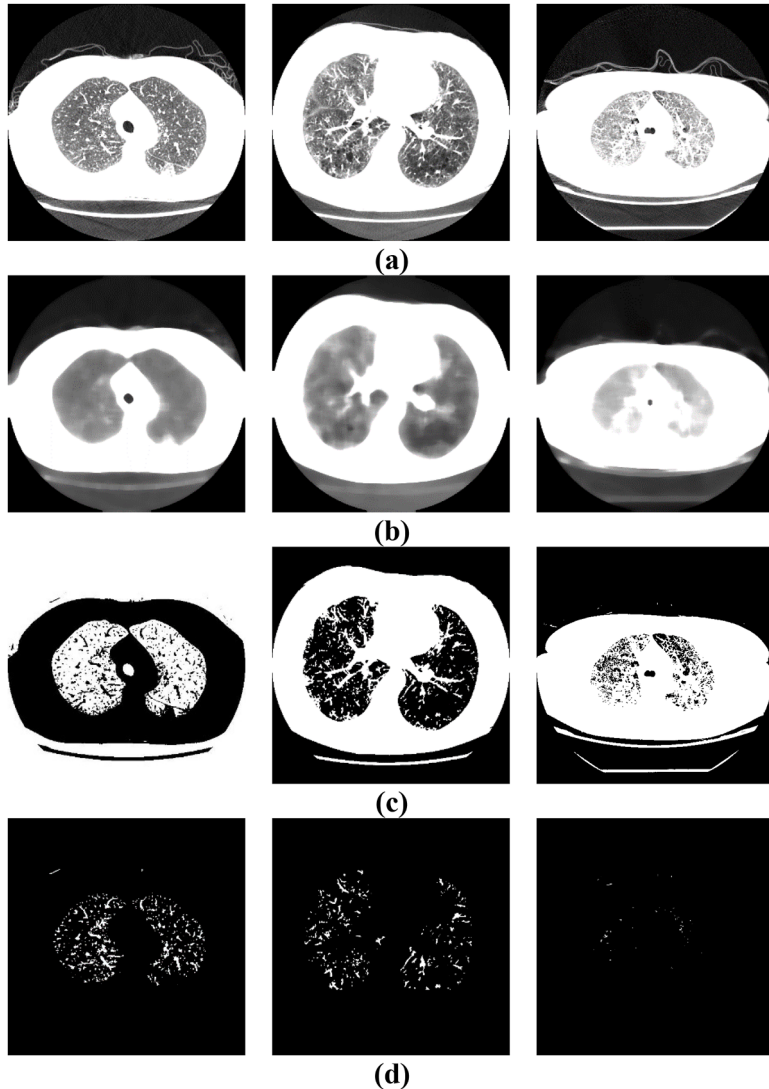


Fig. 6. Image results of SpiLenet based on LIDC-IDRI dataset, a) Input images, b) Preprocessed images, c) Lobe segmented images, d) Node identified images.

3.7. Severity level classification utilizing SpileNet

The severity level possibly classifies whether the disease-affected patient's nodules are cancerous or non-cancerous. Furthermore, it possibly spreads within the lungs to nearby structures. Additionally, early medical care and timely detection are essential, which

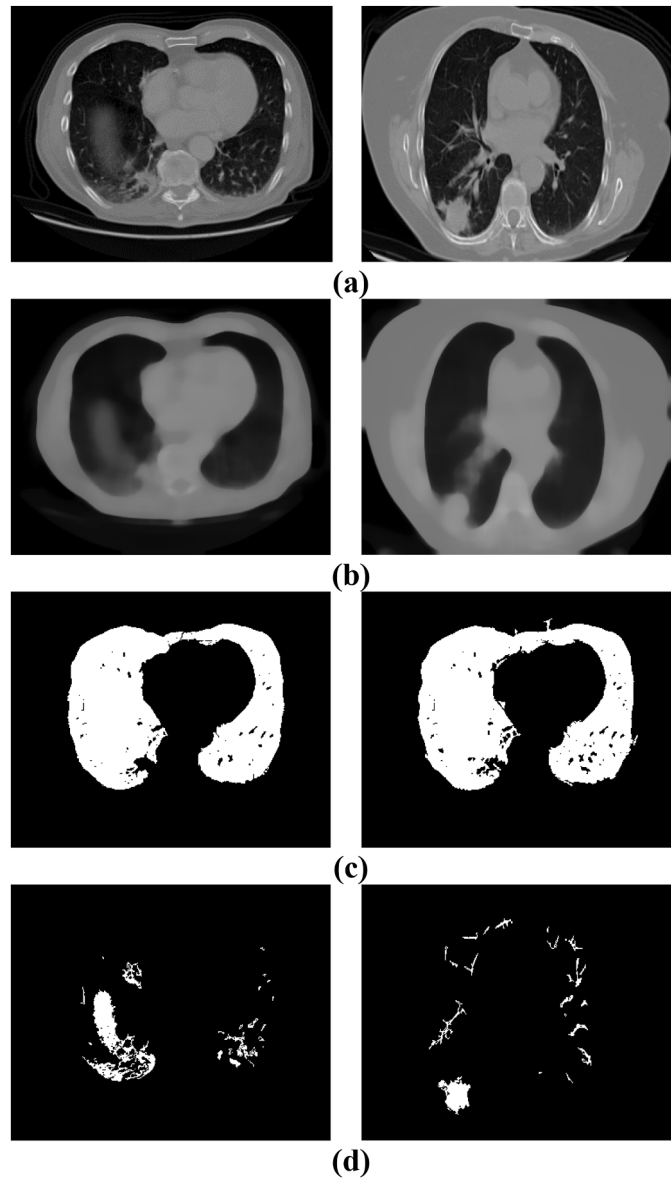


Fig. 7. Experimental results of the SpiLenet using Classification of Lung Cancer CT Images dataset, a) Input images, b) Preprocessed images, c) Lobe segmented images, d) Node identified images.

prevents the spreading of lung cancer. Moreover, lung cancer classification is divided into three types such as moderate, mild, and severe. Based on severity level, clinicians can provide personalized treatment to patients in time. Here, the categorization of severity level for lung cancer is conducted utilizing SpiLenet, where the process is similar to the detection of lung cancer, which is already discussed in [Section 3.6](#).

4. Results and discussion

The outcomes of SpiLenet are demonstrated based on evaluation metrics namely Accuracy, F-measure and recall are described below.

4.1. Experimental setup

The SpiLenet model is accomplished using a Python. [Table 1](#) illustrates the details of the parameter of devised model.

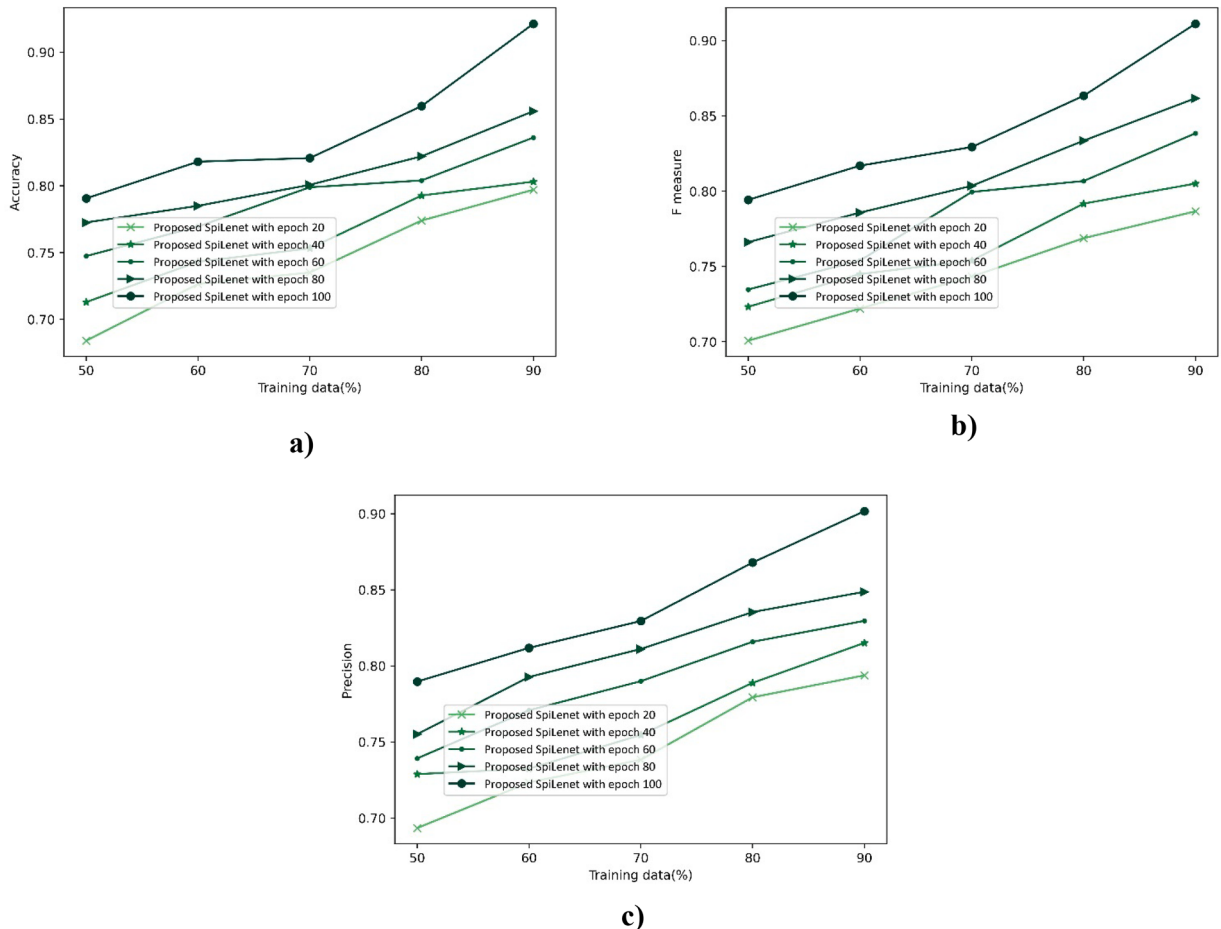


Fig. 8. Performance analysis of SpiLenet model by adjusting training data, a) Accuracy, b) F-measure and c) Precision.

4.2. Experimental outcome

This section presents the experimental results of the proposed model, using the LIDC-IDRI dataset and the Classification of Lung Cancer CT Images dataset.

4.2.1. Experimental outcomes of LIDC-IDRI database

The attained outcome of SpiLenet for Lung cancer detection based on LIDC-IDRI dataset is portrayed in Fig. 6. The input images are described in Fig. 6a), preprocessed images are represented in Fig. 6b), lobe segmented images are displayed in Fig. 6c) and node identified images are specified in Fig. 6d).

4.2.2. Experimental results of classification of lung cancer CT images dataset

The results of SpiLenet for lung cancer detection utilizing the Classification of Lung Cancer CT Images dataset is displayed in Fig. 7. Fig. 7a) illustrates the input images, Fig. 7b) displays the preprocessed images, Fig. 7c) presents the lobe-segmented images, and Fig. 7d) shows the images with identified nodules.

4.3. Dataset description

The detailed description of datasets such as, Lung Image Database Consortium image collection (LIDC-IDRI) dataset, and Classification of Lung Cancer CT Images dataset are explained below:

4.3.1. LIDC-IDRI dataset

The dataset utilized in SpiLenet for identifying Lung cancer is the LIDC-IDRI [15]. With the employment of marked-up annotated lesions and thoracic CT scans, LIDC-IDRI possibly detects entire lung nodules in every CT scan.

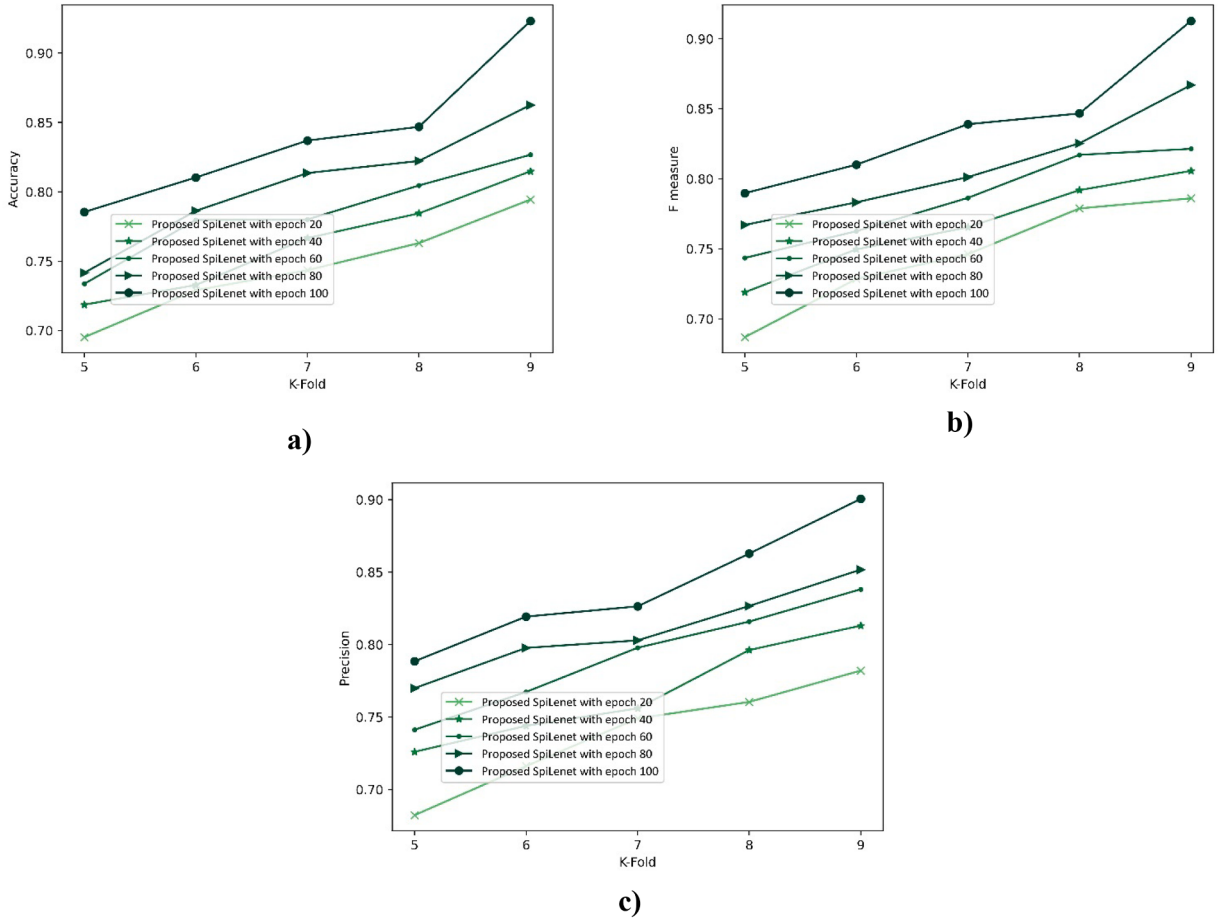


Fig. 9. Performance estimation of SpiLenet model for K-fold, a) Accuracy, b) F-measure and c) Precision.

4.3.2. Classification of lung cancer CT images dataset

The Classification of Lung Cancer CT Images dataset [30] typically refers to a collection of CT scan images of the human lungs, which are used for the purpose of training machine learning models to classify and detect lung cancer. These datasets often include images from various phases of lung cancer such as malignant tumors and benign tumors, and are annotated with labels to help in distinguishing different types of lung abnormalities.

4.4. Evaluation parameters

The Efficaciousness of SpiLenet is evaluated using performance metrics including F-measure, accuracy, and precision.

4.4.1. Accuracy

It precisely detects and classifies the detection rates of lung cancer, which are estimated as,

$$\varphi_1 = \frac{T_p + T_N}{T_p + T_N + N_p + N_N} \quad (54)$$

where, T_p and T_N represents true positive and negative, N_p and N_N refers to false positive and negative lung cancer.

4.4.2. F-measure

It fuses the scores of precision and recall, which is formulated as:

$$\varphi_2 = 2 * \frac{(\varphi_3 * \varphi_4)}{(\varphi_3 + \varphi_4)} \quad (55)$$

where φ_4 denotes as recall.

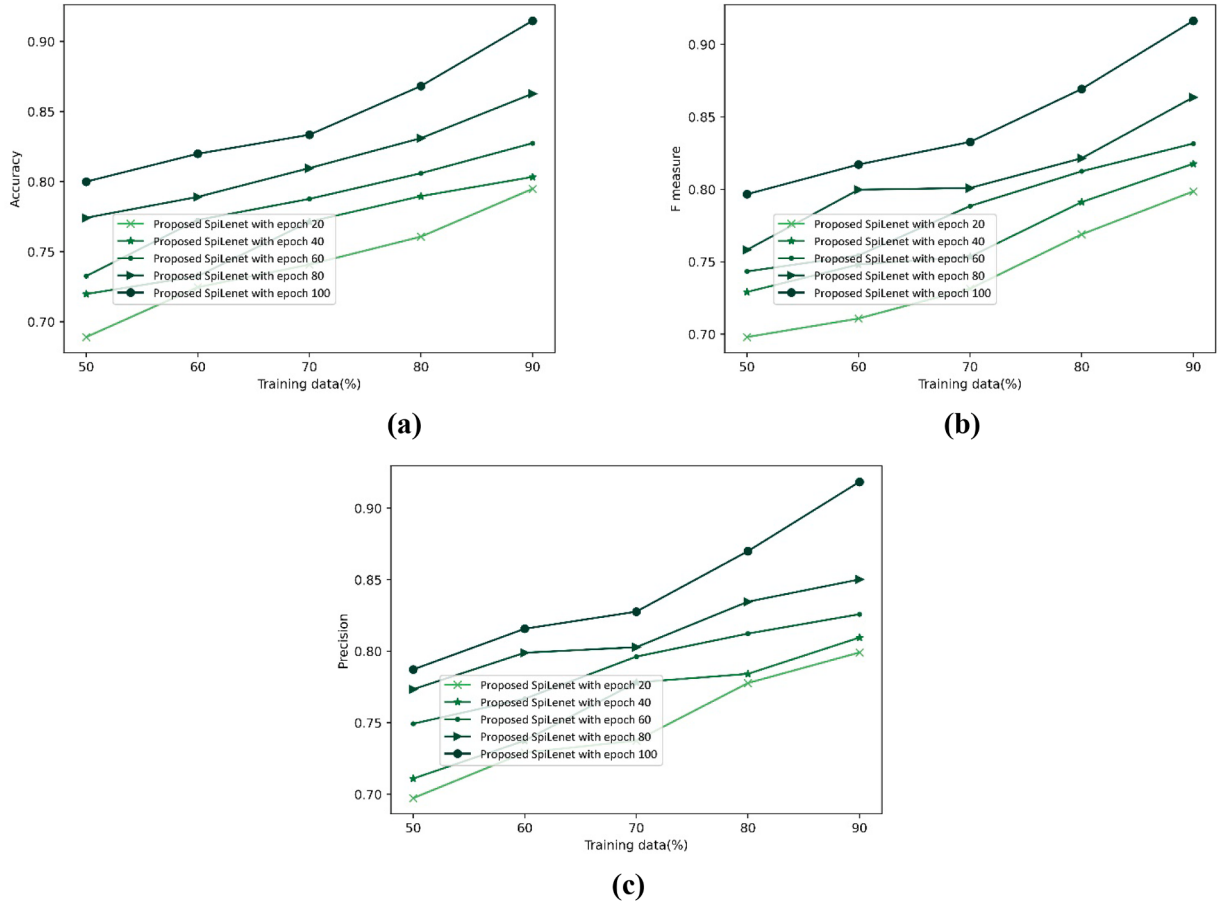


Fig. 10. Performance analysis of SpiLenet model for training data, a) Accuracy, b) F-measure and c) Precision.

4.4.3. Precision

Precision is the ratio of the total number of negative and positive lung cancer observations, and it is calculated as,

$$\phi_3 = \frac{T_p}{T_p + N_p} \quad (56)$$

4.5. Performance analysis

Performance assessment of SpiLenet based on LIDC-IDRI dataset and Classification of Lung Cancer CT Images dataset are described below.

4.5.1. Performance analysis based on LIDC-IDRI dataset

4.5.1.1. By adjusting training data. Performance assessment of SpiLenet for different epochs 20, 40, 60, 80 and 100 is depicted in Fig. 8. Fig. 8a) portrays the evaluation of accuracy. The accuracy of SpiLenet for 90 % of training data is 0.797, 0.803, 0.836, 0.856 and 0.921 for differing epochs 20 to 100, Fig. 8b) indicates the evaluation of SpiLenet regarding F-measure. F-measure of SpiLenet for training data= 90 % by altering epochs 20 to 100 are 0.794, 0.815, 0.830, 0.849 and 0.902. Fig. 8c) displays the evaluation of SpiLenet regarding precision. For 90 % of training data, the precision of SpiLenet by differing epochs from 20 to 100 is 0.787, 0.805, 0.838, 0.862 and 0.911 for the training data is 90 %. Moreover, the designed model demonstrates the higher performance by choosing the relevant features, which leads to detect the lung nodules effectively.

4.5.1.1. By varying K-fold. Assessment of SpiLenet for k-fold by using three evaluation metrics with epochs 20, 40, 60, 80 and 100 is shown in Fig. 9. Investigation of SpiLenet based on accuracy is revealed in Fig. 9a). By varying epochs 20 to 100 SpiLenet attained accuracy by 0.794, 0.815, 0.827, 0.863 and 0.923 for k-fold=9. Analysis of SpiLenet concerning F-measure is exhibited in Fig. 9b). When k-fold=9, F-measure attained by SpiLenet by differing epochs 20 to 100 are 0.782, 0.813, 0.838, 0.852 and 0.901. Fig. 9c) shows the analysis of SpiLenet regarding precision. Considering k-fold=9 SpiLenet achieved precision by 0.786, 0.806, 0.821, 0.867 and

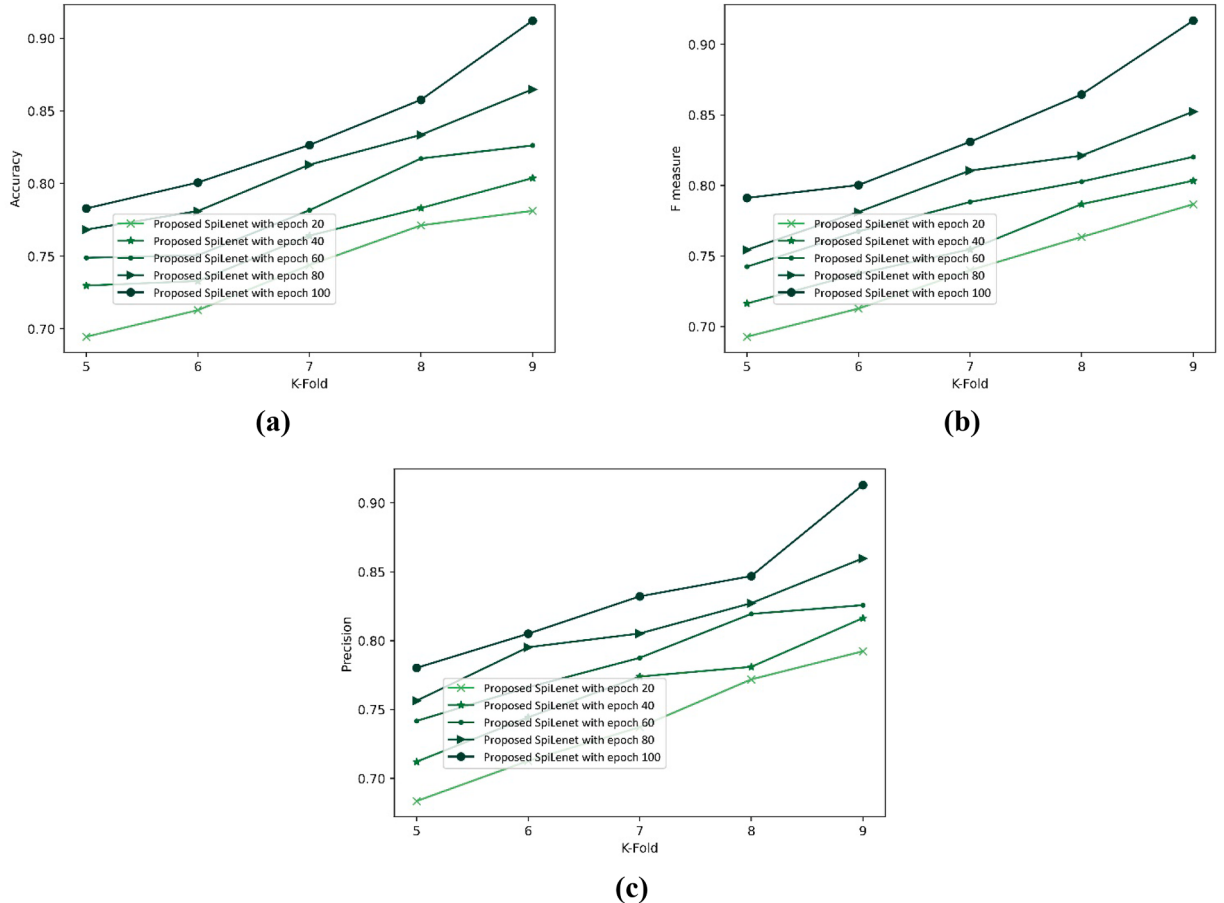


Fig. 11. Performance analysis of SpiLenet model for K-fold, a) Accuracy, b) F-measure and c) Precision.

0.913 for varying epochs from 20 to 100. Furthermore, the proposed model outperforms traditional models by minimizing the number of parameters, resulting in improved computational efficiency.

4.5.2. Performance analysis based on classification of lung cancer CT images dataset

4.5.2.1. By varying training data. Evaluation of SpiLenet in terms of epochs is delineated in Fig. 10. Fig. 10a) displays analysis of SpiLenet in respective to accuracy. For training data is 90 %, the SpiLenet attained the value of accuracy is 0.795, 0.803, 0.827, 0.863, and 0.915 with 20 to 100 epochs. Estimation of SpiLenet with regarding to f-measure is indicated in Fig. 10b). When the training data is 90 %, the f-measure obtained by SpiLenet with 20 to 100 epochs is 0.799, 0.810, 0.826, 0.850, and 0.918. Fig. 10c) mentions estimation of SpiLenet concerning precision. For 90 % of training data, the SpiLenet acquired precision of 0.799 for 20 epoch, 0.818 for 40 epoch, 0.832 for 60 epoch, 0.864 for 80 epoch, and 0.916 for 100 epoch. Additionally, the proposed scheme is especially advantageous for large medical imaging datasets, as it helps decrease both training times and memory demands.

4.5.2.2. By varying k-fold. Fig. 11 depicts the valuation of SpiLenet with various epochs. Assessment of SpiLenet regarding accuracy is implied in Fig. 11a). When considered k-fold=9, the accuracy acquired by SpiLenet with 20, 40, 60, 80, and 100 epochs are 0.781, 0.804, 0.826, 0.865, and 0.912. Fig. 11b) displays the assessment of SpiLenet considering f-measure. For the K-fold is 9, the SpiLenet achieved f-measure values about 0.792 for 20 epoch, 0.816 for 40 epoch, 0.826 for 60 epoch, 0.860 for 80 epoch, and 0.913 for 100 epoch. Fig. 11c) shows analysis of SpiLenet in respective to precision. For the K-fold is 9, the devised SpiLenet acquired precision of 0.787, 0.803, 0.820, 0.852, and 0.917 with 20, 40, 60, 80, and 100 epochs. Subsequently, the devised scheme achieved superior results by capturing hierarchical features, enabling it to effectively differentiate between cancerous and non-cancerous tissue.

4.6. Comparative methods

Comparative methods utilized for assessing the performance of SpiLenet are Improved DNN [2], DGMM-RBCNN [8], DCNN [10] and HSEFS [7].

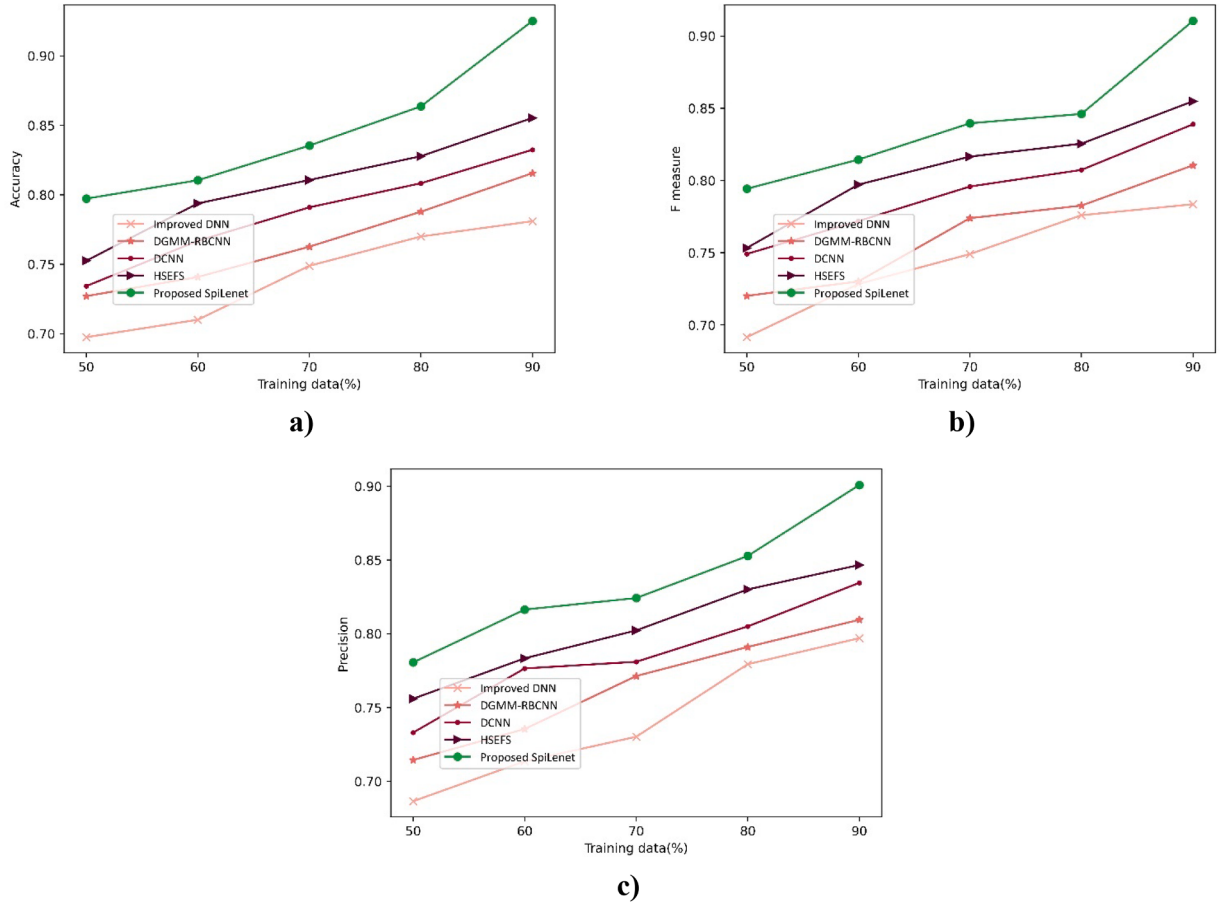


Fig. 12. Comparative estimation of SpiLenet based on training data, a) Accuracy, b) F-measure and c) Precision.

4.7. Comparative analysis

A comparative study of SpiLenet using the LIDC-IDRI dataset [15] and Classification of Lung Cancer CT Images dataset [30] by varying training data and k-fold is explained in this section.

4.7.1. Comparative estimation based on LIDC-IDRI dataset

4.7.1.1. Concerning the training data. Fig. 12 demonstrates the analysis of SpiLenet by differing training data. Fig. 12a) reveals the investigation of SpiLenet concerning accuracy. Accuracy of Improved DNN, DGMM-RBCNN, DCNN, HSEFS and SpiLenet are 0.781, 0.816, 0.832, 0.855 and 0.925 for training data=90 %. SpiLenet outperformed Improved DNN, DGMM-RBCNN, DCNN and HSEFS by 15.580 %, 11.841 %, 10.025 % and 7.547 %. Evaluation of SpiLenet regarding F-measure is portrayed in Fig. 12b). The F-measure of conventional strategies for 90 % of training data is 0.797, 0.810, 0.835 and 0.847, whereas the F-measure attained by SpiLenet is 0.901. Moreover, the enhanced performance of SpiLenet over existing schemes is 11.532 %, 10.143 %, 7.365 % and 6.019 %. Fig. 12c) portrays an examination of SpiLenet concerning precision. The precision of traditional approaches is 0.784, 0.810, 0.839 and 0.855, while SpiLenet has a precision of 0.910 for the training data is 90 %. Here, the designed model achieved better results by effectively addresses complex clinical segmentation challenges while preserving computational efficiency.

4.7.1.2. By adjusting K-fold. Fig. 13 portrays the investigation of SpiLenet by varying the k-fold. Evaluation of accuracy is represented in Fig. 13a). For, the K-fold is 9, the accuracy achieved by SpiLenet is 0.921, while Improved DNN, DGMM-RBCNN, DCNN and HSEFS have gained accuracy of 0.789, 0.818, 0.837 and 0.864. Thus, the increased performance of SpiLenet with conventional strategies is 14.338 %, 11.235 %, 9.207 % and 6.254 %. Fig. 13b) shows an investigation of SpiLenet regarding F-measure. When K-fold=9 Improved DNN, DGMM-RBCNN, DCNN, HSEFS and SpiLenet have F-measures of 0.800, 0.812, 0.822, 0.847 and 0.904. The SpiLenet outperforms competing techniques by 11.560 %, 10.205 %, 9.054 % and 6.358 %. Fig. 13c) represents the assessment of SpiLenet in terms of precision. The precision of SpiLenet is 0.911, Improved DNN is 0.793, DGMM-RBCNN is 0.809, DCNN is 0.837 and HSEFS is 0.847. Here, SpiLenet yields performance improvement by 12.926 %, 11.168 %, 8.144 % and 7.043 % for the k-fold is 9. Furthermore,

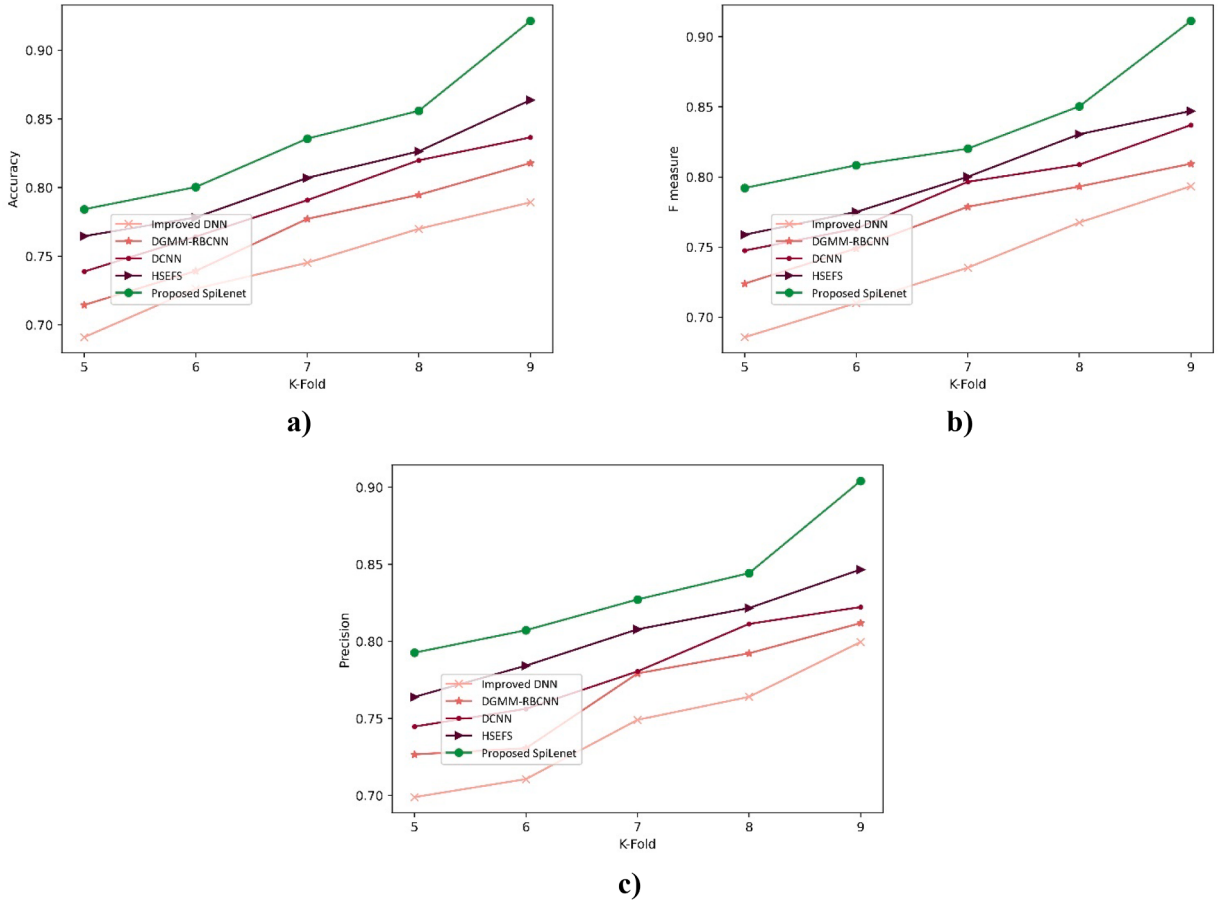


Fig. 13. Comparative estimation of SpiLenet for k-fold, a) Accuracy, b) F-measure and c) Precision.

the devised scheme improves the performance, making it more dependable for clinical decision-making.

4.7.2. Comparative analysis based on classification of lung cancer CT images dataset

4.7.2.1. Regarding the training data. The evaluation of SpiLenet model by considering Classification of Lung Cancer CT Images Dataset is portrayed in Fig. 14. The accuracy-based investigation of SpiLenet is illustrated in Fig. 14(a). Here, the approaches, such as Improved DNN, DGMM-RBCNN, DCNN and HSEFS attained the accuracy of 0.798, 0.804, 0.823, and 0.841, when the training data is 90 %, while SpiLenet calculated an accuracy of 0.916. This shows that the proposed SpiLenet has enhanced the performance by 12.88 %, 12.24 %, 10.15, and 8.19 %. Fig. 14(b) shows the analysis of SpiLenet by employing f-measure. The SpiLenet approach measured a f-measure of 0.912 for the training data is 90 %. Meanwhile, the other approaches, namely Improved DNN, DGMM-RBCNN, DCNN and HSEFS acquired a f-measure of 0.791, 0.816, 0.829, and 0.860, respectively. It shows that the performance improvement of the proposed model is 13.27 %, 10.53 %, 9.10 %, and 5.70 %. The valuation of SpiLenet method with precision in terms of training data is depicted in Fig. 14(c). If the training data is 90 %, the precision of Improved DNN is 0.786, DGMM-RBCNN is 0.809, DCNN is 0.830, and HSEFS is 0.857, and SpiLenet is 0.916. Thus, the performance improvement of the SpiLenet with other methods is 14.19 %, 11.68 %, 9.39 %, and 6.44 %. In conclusion, the designed scheme demonstrated superior performance by effectively combines features, which also efficiently handles large datasets, and reduces the computational effort.

4.7.2.2. By regarding K-fold. The examination of SpiLenet technique by assuming Classification of Lung Cancer CT Images dataset is displayed in Fig. 15. The assessment of SpiLenet with accuracy is exemplified in Fig. 15(a). For the k-fold is 9, SpiLenet calculated an accuracy of 0.917, and the accuracy obtained by other approaches, like Improved DNN, DGMM-RBCNN, DCNN and HSEFS, are 0.790, 0.814, 0.821, and 0.857. Furthermore, the performance of SpiLenet is improved by 13.85 %, 11.23 %, 10.47 %, and 6.54 %. Fig. 15(b) exposes the valuation of SpiLenet with f-measure based on k-fold. Here, when k-fold is 9, the f-measure of Improved DNN is 0.784, DGMM-RBCNN is 0.813, DCNN is 0.838, and HSEFS is 0.856, and SpiLenet is 0.917. The significant improvement of SpiLenet compared with other techniques is 14.50 %, 11.34 %, 8.62 %, and 6.65 %. The graph among the precision and k-fold is represented in Fig. 15(c). At k-fold 9, the precision recorded by SpiLenet is 0.911, while the precision values attained by existing approaches, like

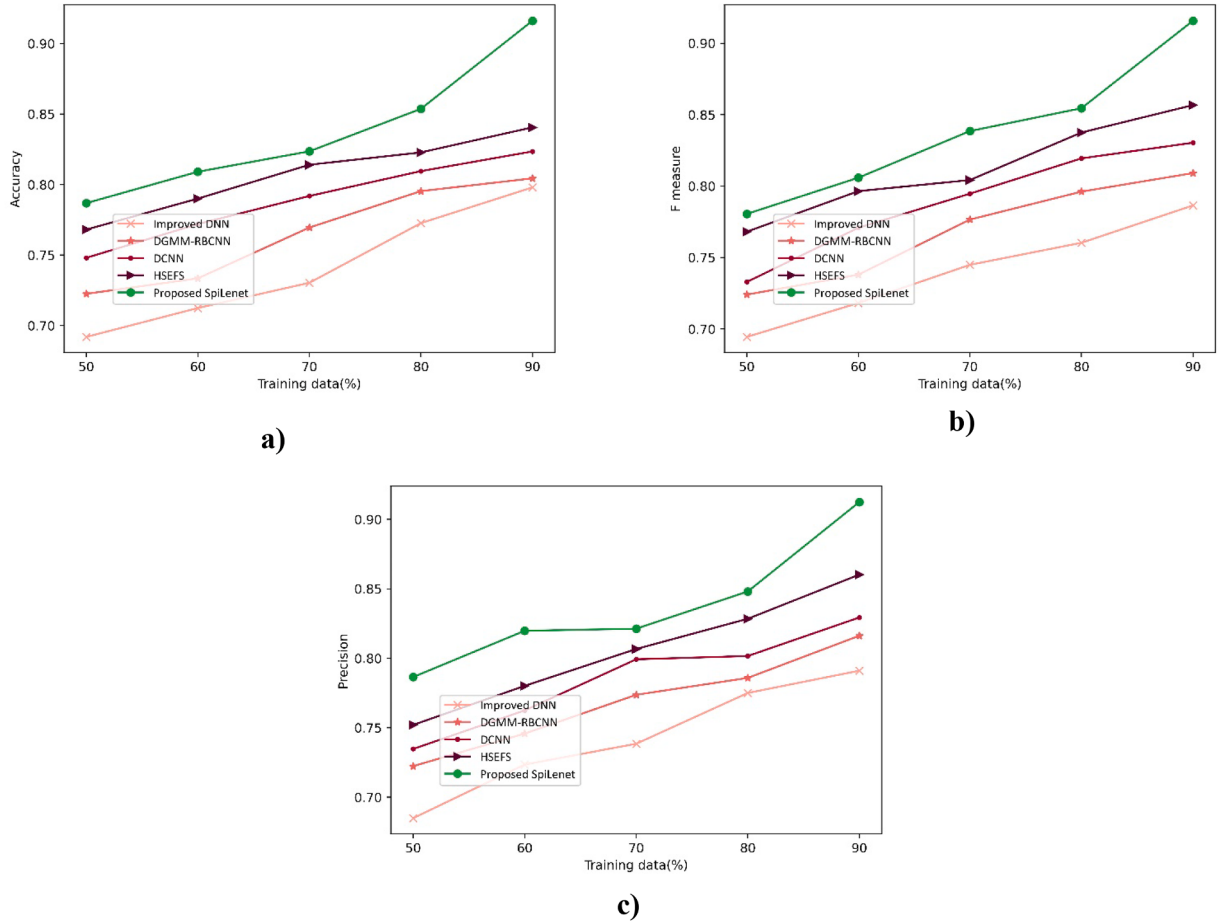


Fig. 14. Comparative estimation of SpiLenet by adjusting the training data, a) Accuracy, b) F-measure and c) Precision.

Improved DNN, DGMM-RBCNN, DCNN and HSEFS are 0.798, 0.803, 0.822, and 0.865. Thus, it illustrates that the performance of SpiLenet is enhanced by 12.40 %, 11.86 %, 9.77 %, and 5.05 %. Furthermore, the designed scheme achieved optimal results by effectively managing fine-scale variations in the data, making it particularly well-suited for high-resolution imaging.

4.8. Comparative discussion

Table 2 demonstrates a comparative discussion of SpiLenet, where analysis is executed using LIDC-IDRI and Classification of Lung Cancer CT Images datasets, by concerning the training data and k-fold. When the k-fold is 9, the devised SpiLenet has attained highest accuracy of 92.1 %, and then, the previous models recorded the accuracy of 78.9 %, 81.8 %, 83.7 %, and 86.4 % for Improved DNN, DGMM-RBCNN, DCNN and HSEFS. Similarly comparing it with conventional approaches SpiLenet has attained maximum F-measure of 90.4 %, whereas, the traditional models such as, Improved DNN, DGMM-RBCNN, DCNN and HSEFS measured the f-measure of 80.0 %, 81.2 %, 82.2 %, and 84.7 %. Subsequently, the proposed model achieved the precision of 91.1 %, while, the conventional models gained the precision of 79.3 % for Improved DNN, 80.9 % for DGMM-RBCNN, 83.7 % for DCNN, and 84.7 % for HSEFS. Hence, it is proved that SpiLenet precisely detects lung cancer with the highest detection rate. Thus, it is more precise and efficient. Further, it requires lower training time and has higher detection accuracy.

4.9. Analysis based on features

Fig. 16 illustrates the analysis based on features across two datasets by adjusting the training data. Fig. 16a) depicts the accuracy analysis based on features using LIDC-IDRI dataset. For the training data is 90 %, the devised SpiLenet model with all features achieved the accuracy value of 0.881, while the features such as, SpiLenet with LDN, MTP, MRELBP and statistical features measured the accuracy of 0.789, 0.808, 0.826, and 0.848. Fig. 16b) shows the assessment based on features regarding Classification of Lung Cancer CT Images dataset. If the training data is 90 %, the accuracy recorded by SpiLenet with LDN is 0.791, MTP is 0.810, MRELBP is 0.821, statistical features is 0.860, and the proposed SpiLenet with all features is 0.897.

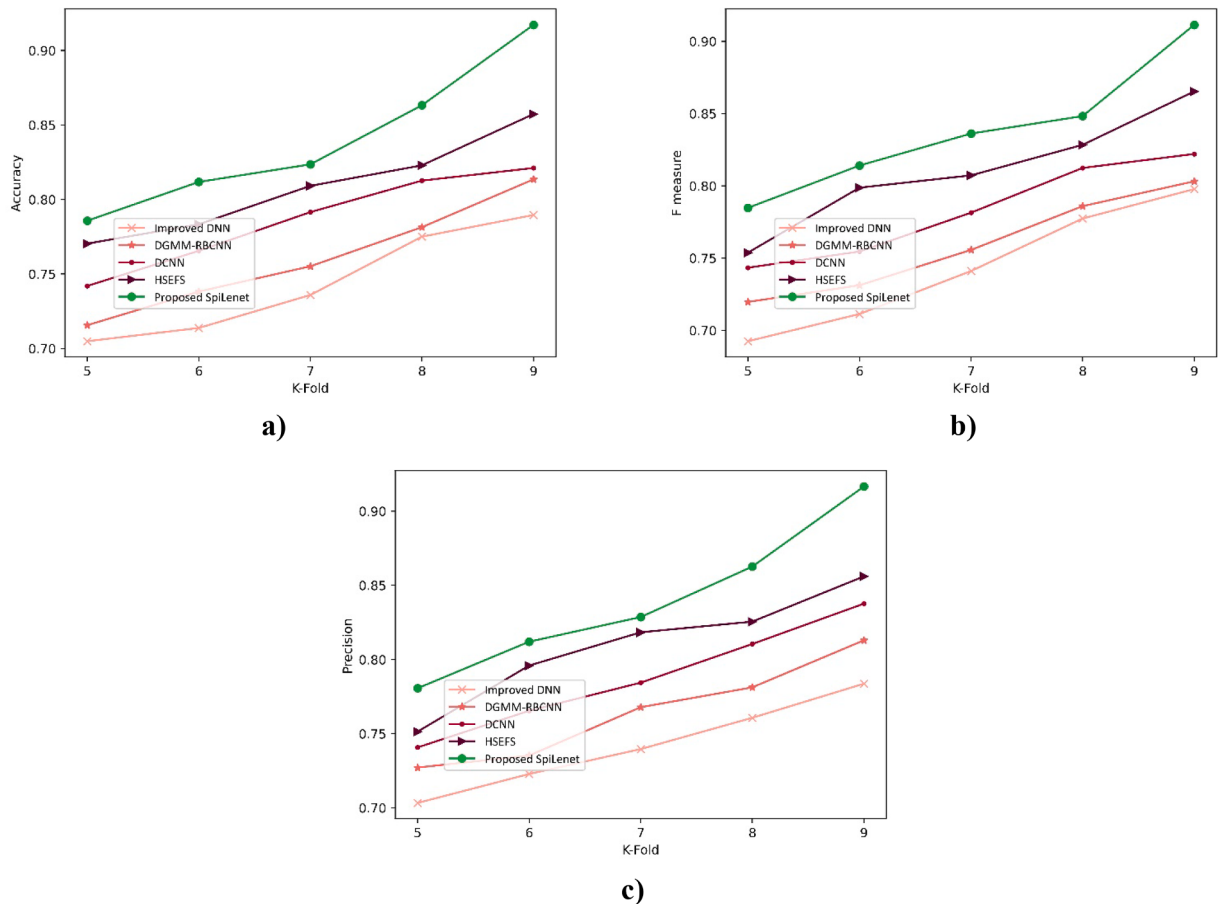


Fig. 15. Comparative assessment of SpiLenet for K-fold, a) Accuracy, b) F-measure and c) Precision.

Table 2
Comparative discussion.

Setup	Metrics Based on LIDC-IDRI dataset	Improved DNN	DGMM-RBCNN	DCNN	HSEFS	Proposed SpiLenet
Training data=90 %	Accuracy (%)	78.1	81.6	83.2	85.5	92.5
	F-measure (%)	79.7	81.0	83.5	84.7	90.1
	Precision (%)	78.4	81.0	83.9	85.5	91.0
K-fold=9	Accuracy (%)	78.9	81.8	83.7	86.4	92.1
	F-measure (%)	80.0	81.2	82.2	84.7	90.4
	Precision (%)	79.3	80.9	83.7	84.7	91.1
Based on Classification of Lung Cancer CT Images dataset						
Training data=90 %	Accuracy (%)	79.8	80.4	82.3	84.1	91.6
	F-measure (%)	79.1	81.6	82.9	86.0	91.2
	Precision (%)	78.6	80.9	83.0	85.7	91.6
K-fold=9	Accuracy (%)	79.0	81.4	82.1	85.7	91.7
	F-measure (%)	78.4	81.3	83.8	85.6	91.7
	Precision (%)	79.8	80.3	82.2	86.5	91.1

4.10. Failure analysis

Table 3 presents the analysis of failure cases in the dataset. In this table, the normal classes are labeled as '0' and the abnormal classes as '1'. The normal classes comprise 413 images, in which 14 identified as failure cases. Subsequently, the abnormal classes include 605 images, in which 11 identified as failure cases. The failure cases in the normal class are attributed to incomplete annotations and resolutions, while the failure cases in the abnormal class are due to nodules being <3mm.

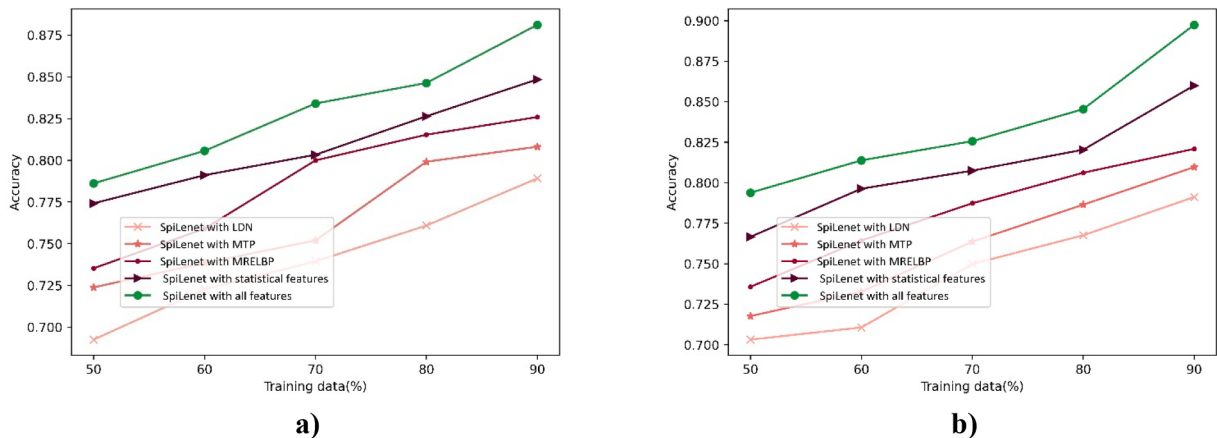


Fig. 16. Assessment of features using accuracy based on (a) LIDC-IDRI dataset, (b) Classification of Lung Cancer CT Images dataset.

Table 3
Analysis of failure cases.

No. of classes	Total no of images	Failure cases
0	413	14
1	605	11

Table 4
Analysis of computational time.

Time	Improved DNN	DGMM-RBCNN	DCNN	HSEFS	Proposed SpiLenet
Based on LIDC-IDRI dataset					
Training time (min)	10.259	9.349	8.987	7.878	6.987
Testing time (sec)	8.350	7.982	6.294	5.982	3.986
Based on Classification of Lung Cancer CT Images dataset					
Training time (min)	12.462	11.565	9.958	8.746	6.066
Testing time (sec)	9.457	8.755	7.765	6.655	5.465

4.11. Assessment of computational time

Table 4 represents the evaluation of computational time. It is the amount of time required by a computer or system to perform a specific task or set of tasks. Also, it can refer to the total time spent on both training and testing a model, especially in the context of machine learning or deep learning tasks. Here, when compared to other existing models, the designed model attained the minimal computational time.

5. Conclusion

Recently, the mortality rate of lung cancer has been observed as the highest of all cancer kinds. Annually, Lung cancer has a gradual increase in death with minimal survival rate after diagnosis. However, the patient's survival rate is directly dependent upon its identification period. Moreover, there is a highest possibility of survival if the Lung cancer is identified initially. Hence this research developed the SpiLenet for Lung cancer detection. Initially, the CT input images are pre-processed by utilizing an SG filter. In addition, the segmentation is performed by DRINet. Lastly, Lung cancer detection is executed using SpiLenet, which is the hybridization of SpinalNet and LeNet. Furthermore, experimental results of SpiLenet have yielded a highest Accuracy of 92.10 %, F-measure of 90.40 % and Precision of 91.10 %. The proposed model significantly enhances the likelihood of successful treatment by detecting lung cancer at an early stage. Also, the devised scheme improves the quality of life for patients by minimizing the severity of symptoms and the side effects of treatment. However, the proposed model suffers from limitations in terms of the size and quality of labeled data, especially for rare stages or subtypes of cancer. Deep learning models, including SpinalNet and LeNet, require large, high-quality datasets to train effectively. Insufficient data may lead to overfitting or poor generalization. Also, the differences in patient demographics and imaging conditions can affect model performance. In the future, a potential direction for this research is to explore the use of hybrid networks combined with hybrid optimization techniques to further enhance accuracy in lung cancer detection. Also, the future research will explore the Few-shot learning techniques to identify lung cancer from only a few examples, which could be valuable in cases of rare cancer subtypes or early-stage lung cancer, where labeled data is limited. Moreover, future study will investigate the use of generative

models to generate synthetic lung cancer images for training deep learning models to address data imbalance issues.

Declaration of competing interest

The authors declare that they have no conflict of interest.

Data availability

No data was used for the research described in the article.

References

- [1] Hong Y, Hong SH, Oh YM, Shin SH, Choi SS, Kim WJ. Identification of lung cancer-specific differentially methylated regions using genome-wide DNA methylation study. *Mol Cell Toxicol* 2018;14:315–22.
- [2] Shakeel PM, Burhanuddin MA, Desai MI. Automatic lung cancer detection from CT image using improved deep neural network and ensemble classifier. *Neural Comput Appl* 2022;1–14.
- [3] Alzubaidi MA, Otoom M, Jaradat H. Comprehensive and comparative global and local feature extraction framework for lung cancer detection using CT scan images. *IEE Access* 2021;9:158140–54.
- [4] Travis WD. Pathology of lung cancer. *Clin Chest Med* 2011;32(4):669–92.
- [5] Makaju S, Prasad PWC, Alsadoon A, Singh AK, Elchouemi A. Lung cancer detection using CT scan images. *Procedia Comput Sci* 2018;125:107–14.
- [6] Thun MJ, Hannan LM, Adams-Campbell LL, Boffetta P, Buring JE, Feskanich D, Flanders WD, Jee SH, Katanoda K, Kolonel LN, Lee IM. Lung cancer occurrence in never-smokers: an analysis of 13 cohorts and 22 cancer registry studies. *PLoS Med* 2008;5(9):e185.
- [7] Bishnoi V, Goel N, Tayal A. Wrapper-based best feature selection approach for lung cancer detection. In: Artificial Intelligence and Sustainable Computing for Smart City", First International Conference, AIS2C2 2021, Greater Noida, India, Revised Selected Papers 1. Springer International Publishing; 2021. p. 175–86.
- [8] Jena SR, George ST, Ponraj DN. Lung cancer detection and classification with DGMM-RBCNN technique. *Neural Comput Appl* 2021;33:15601–17.
- [9] Vijh S, Gaurav P, Pandey HM. Hybrid bio-inspired algorithm and convolutional neural network for automatic lung tumor detection. *Neural Comput Appl* 2023; 35(33):23711–24.
- [10] Tiwari L, Awasthi V, Patra RK, Miri R, Raja H, Bhaskar N. Lung cancer detection using deep convolutional neural networks. In: Data Engineering and Intelligent Computing: Proceedings of 5th ICICC 2021. 1. Singapore: Springer Nature Singapore; 2022. p. 373–85.
- [11] Riquelme D, Akhlefoui MA. Deep learning for lung cancer nodules detection and classification in CT scans. *Ai* 2020;1(1):28–67.
- [12] Chaudhary A, Singh SS. Lung cancer detection on CT images by using image processing. In: 2012 International Conference on Computing Sciences. IEEE; 2012. p. 142–6. September.
- [13] Nazir I, Haq IU, Khan MM, Qureshi MB, Ullah H, Butt S. Efficient pre-processing and segmentation for lung cancer detection using fused CT images. *Electronics* 2021;11(1):34.
- [14] Tiwari L, Raja R, Awasthi V, Miri R, Sinha GR, Alkinani MH, Polat K. Detection of lung nodule and cancer using novel Mask-3 FCM and TWEDLNN algorithms. *Measurement* 2021;172:108882.
- [15] Lung cancer detection using CT scan images dataset is taken from, "<https://wiki.cancerimagingarchive.net/display/Public/LIDC-IDRI>", accessed on December 2023.
- [16] Liu Y, Dang B, Li Y, Lin H, Ma H. Applications of Savitzky-Golay filter for seismic random noise reduction. *Acta Geophysica* 2016;64:101–24.
- [17] Chen L, Bentley P, Mori K, Misawa K, Fujiwara M, Rueckert D. DRINet for medical image segmentation. *IEE Trans Med Imaging* 2018;37(11):2453–62.
- [18] Chinniah P, Maram B, Velrajkumar P, Vidyadhari C. DeepJoint segmentation-based lung segmentation and hybrid optimization-enabled deep learning for lung nodule classification. *Intern J Pattern Recogn Artif Intell* 2022;36(13):2252021.
- [19] Al-Nabki MW, Fidalgo E, Alegre E, Fernandez-Robles L. Improving named entity recognition in noisy user-generated text with local distance neighbor feature. *Neurocomputing* 2020;382:1–11.
- [20] Bashar F, Khan A, Ahmed F, Kabir MH. Robust facial expression recognition based on median ternary pattern (MTP). In: 2013 International Conference on Electrical Information and Communication Technology (EICT). IEEE; 2014. p. 1–5. February.
- [21] Barburiceanu S, Terebes R, Meza S. Hyperspectral Image Classification using the MRELBP Texture Descriptor. In: 2019 E-Health and Bioengineering Conference (EHB). IEEE; 2019. p. 1–6. November.
- [22] Kabir HD, Abdar M, Khosravi A, Jalali SMJ, Atiya AF, Nahavandi S, Srinivasan D. Spinalnet: deep neural network with gradual input. *IEEE Trans Artif Intell* 2022.
- [23] Al-Jawfi R. Handwriting Arabic character recognition LeNet using neural network. *Int Arab J Inf Technol* 2009;6(3):304–9.
- [24] Rivera AR, Castillo JR, Chae OO. Local directional number pattern for face analysis: face and expression recognition. *IEEE Trans Image Process* 2012;22(5): 1740–52.
- [25] Khan A, Bashar F, Ahmed F, Kabir MH. Median ternary pattern (MTP) for face recognition. In: 2013 International Conference on Informatics, Electronics and Vision (ICIEV). IEEE; May 2013. p. 1–5.
- [26] Lessa V, Marengoni M. Applying artificial neural network for the classification of breast cancer using infrared thermographic images. In: Computer Vision and Graphics: International Conference, ICCVG 2016, Warsaw, Poland, Proceedings. Springer International Publishing; 2016. p. 429–38. September 19–21.
- [27] Wei G, Li G, Zhao J, He A. Development of a LeNet-5 gas identification CNN structure for electronic noses. *Sensors* 2019;19(1):217.
- [28] Ishibuchi H, Nozaki K, Yamamoto N, Tanaka H. Construction of fuzzy classification systems with rectangular fuzzy rules using genetic algorithms. *Fuzzy Sets Syst* 1994;65(2–3):237–53.
- [29] Ryu J. Improved image quality assessment by utilizing pre-trained architecture features with unified learning mechanism. *Appl Sci* 2023;13(4):2682.
- [30] Classification of Lung Cancer Computed Tomography Images dataset is taken from, "<https://figshare.com/articles/dataset/Mahesswari/23741562>", accessed on October 2024.